Modeling and simulation of blood circulation and perfusion

Ulin Nuha Abdul Qohar

Thesis for the degree of Philosophiae Doctor (PhD)
University of Bergen, Norway
2023

UNIVERSITY OF BERGEN

Modeling and simulation of blood circulation and perfusion

Ulin Nuha Abdul Qohar

Thesis for the degree of Philosophiae Doctor (PhD)
at the University of Bergen

Date of defense: 16.06.2023

Year: 2023

Title: Modeling and simulation of blood circulation and perfusion

Name: Ulin Nuha Abdul Qohar

Print: Skipnes Kommunikasjon / University of Bergen

Preface

This thesis is submitted as a partial fulfillment of the requirements for the degree of Philosophiae Doctor (Ph.D.) at the University of Bergen. This study was carried out at the Department of Mathematics, University of Bergen. The Ph.D. project has been financially supported by the Research Council of Norway, FBI-DC project, grant number 262203.

The advisory committee

- Antonella Zanna Munthe-Kaas (University of Bergen)
- Jan M. Nordbotten (University of Bergen)
- Erik Andreas Hanson (Western Norway University of Applied Sciences)

Acknowledgements

I would like to thank my supervisors Antonella Zanna Munthe-Kaas, Jan Martin Nordbotten, and Erik Andreas Hanson for their encouraging, helpful, positive, and constructive advice. Thanks to our meeting, your feedback, and our good talks. It is highly appreciated, and I should probably have asked for your advice more often.

I would also like to thank Steven Sourbron and his group at the Department of Infection, Immunity and Cardiovascular Disease at the University of Sheffield, for letting me visit them and for making my stays there both pleasant and valuable for sharing their insight with me.

Also thanks to the whole FBI-DC project team. It has been nice getting to know all of you, both in a scientific and social setting. I would further express my thanks to the Department of Mathematics, it has served me an invaluable experience and been a great place to work.

Finally, I would also like to thank my wife Ila and our children for the great times we always have together and my family and friends for always being inspiring supporters. A special thanks to my parents for your advice and kindness, I am extremely grateful.

Ulin Nuha Abdul Qohar
Oslo, January 2023

Abstract

Numerical simulations have become essential for understanding blood circulation and perfusion, as well as providing important insights for medical applications. More realistic models have become possible with technological advances, not only in the form of more complex physics, but also in the flow detail of an entire organ circulation. These characteristics are frequently of interest because blood vessels at different spatial scales have different physiological properties.

This thesis focuses on the modeling and simulations of blood flow, tracer transport, and perfusion in an organ tissue. The physical processes are expressed in a multiscale flow model with segmented arteries and veins forming a vascular network flow model that is connected to a microcirculation model. The unobservable vasculature, including small vessels and capillaries, represented by the connection model, is simulated by using a continuum and discrete approach.

A multiscale framework for solving blood circulation is presented. The novelty of this framework comes from combining an existing hybrid flow model for a multiscale circulation with vasculature-induced nonlinearities such as vessel wall elasticity and vessel curvature. By using an appropriate linear algebra precondition, the corresponding nonlinear system can be efficiently solved by using an iterative Newton method. This allows us to formulate more realistic blood circulation in a complex physical domain by employing a relatively simple framework with a low computational cost.

The models and their implementation are presented in the papers that constitute Part II of this thesis. In the paper section, we propose a framework to generate a digital phantom for perfusion imaging. Moreover, we evaluate tracer kinetic models demonstrating the significant value of post-processing of medical data. We also investigate optimal vascular networks revealing a complex interdependence between the geometry of the vascular network, the capillary bed and organ shape.

The results of this thesis contribute to a better understanding of blood perfusion models in tissue and their potential, as well as the potential of scientific computing, for medical applications not limited to perfusion imaging.

Sammendrag

Numeriske simuleringer har hatt vesentlig betydning for vår forståelse av perfusjon og blodsirkulasjon, og simuleringer gir også viktig innsikt under utviklingen av medisinske anvendelser. Teknologiske fremskritt har muliggjort bruken av mer realistiske modeller, ikke bare i form av mer kompleks fysikk, men også ved at en kan studere sirkulasjonen i hele organer. Disse kjennetegnene er ofte av interesse da fysiologiske egenskaper er forskjellige på tvers av romlige størrelsesordener.

Denne avhandlingen fokuserer på modellering og simulering av blodstrøm, sporstofftransport og perfusjon i organvev. De fysiske prosessene er uttrykt i en flerskala strømningsmodell der segmenterte arterier og vener danner en nettverksmodell for vaskulær strømning, og som er knyttet til en mikrosirkulasjonsmodell. Den ikkeobserverbare vaskulaturen beskrevet av modellen simuleres både med en kontinuerlig og en diskretisert tilnærming.

Vi presenterer et flerskala rammeverk for å studere blodsirkulasjon. Det nytenkende aspektet ved rammeverket består i å kombinere en eksisterende hybrid strømningsmodell for flerskala sirkulasjon med vaskulærfremkalte ikke-lineariteter som har opphav i bl.a. veggelastisiteten og kurvaturen til blodkarene. Anvendelsen av en passende betingelse fra lineær algebra gjør at vi effektivt kan løse det tilknyttede ikke-lineære systemet ved bruk av en iterativ Newtons metode, og det relativt enkle rammeverket beskriver slik blodsirkulasjon i et komplekst fysisk domene med en lav beregningsmessig kostnad.

Modellene og deres tilhørende implementeringer presenteres i artiklene som utgjør Del II i avhandlingen. Her foreslår vi et rammeverk for å generere digitale fantomer for avbildning av perfusjon, og ved å evaluere kinetikkmodeller for sporstoff demonstrerer vi de betydelige verdiene som finnes i etterbehandling av medisinske data. I tillegg undersøker vi optimale vaskulære nettverk som avslører en kompleks gjensidig avhengighet mellom geometrien til det vaskulære nettverket, kapillærene og organene.

Resultatene fra denne avhandlingen bidrar til en bedre forståelse av blodperfusjonsmodeller i vev og potensialet til disse, samt potensialet som vitenskapelig databehandling har i medisinske anvendelser utover perfusjonsavbildning.

List of papers

A **A nonlinear multi-scale model for blood circulation in a realistic vascular system**
Ulin Nuha A. Qohar, Antonella Zanna Munthe-Kaas, Jan Martin Nordbotten and Erik Andreas Hanson
Published in the Royal Society Open Science Journal

B **A multi-scale flow model for studying blood circulation in vascular system**
Ulin Nuha A. Qohar, Antonella Zanna Munthe-Kaas, Jan Martin Nordbotten and Erik Andreas Hanson
Published in proceeding of the European Conference on Numerical Mathematics and Advanced Applications (ENUMATH 2019)

C **Network flow simulation as digital reference in DCE-MRI tracer kinetic model validation**
Ulin Nuha A. Qohar, Steven Sourbron, Antonella Zanna Munthe-Kaas, and Erik Andreas Hanson
Submitted to Magnetic Resonance in Medicine Journal.

D **A Study of Vascular Structure Optimization Using Hybrid Flow Model**
Ulin Nuha A. Qohar, Antonella Zanna Munthe-Kaas, Jan Martin Nordbotten and Erik Andreas Hanson
Preprint

Contents

Part I

Background

Chapter 1

Introduction

The study of blood flow in the human circulatory system has been of great importance in the past couple of centuries. Blood circulation is a complex system that involves vascular vessels at different spatial scales, ranging from arteries to capillaries to veins. Mathematical modeling and numerical simulations are essential for describing the entire vascular system and assessing the risk and benefit of a scenario during surgery. Mathematical models can also aid in the understanding of physical processes in the vascular system and are clinically relevant to a wide range of medical applications.

Patient-specific hemodynamic simulations are typically initiated by acquiring a medical image from an imaging modality [23, 37, 49]. Hence, having complete vasculature image data from an organ is essential. Magnetic resonance imaging (MRI) is a noninvasive, radiation-free imaging modality that generates three-dimensional detailed anatomical images. However, even with a 7T scanner, the resolution limit of an MRI is 250 microns, which is far greater than the radius of capillary vessels [67]. Time-of-flight magnetic resonance angiography (ToF-MRA) acquisition can only identify larger arteries [21], and a quantitative susceptibility map (QSM) allows for the extraction of larger veins [2]. To complete a full blood flow modeling, unobservable vessels, including microvasculature, must be acquired by using another imaging modality or described by using a suitable physical model. It must be said that there are imaging modalities allowing for higher resolution capable to resolve capilaries. However, the shortcoming is that these can cover only small-sized regions/tissues typically formalin-fixed. They are currently not suitable for living organisms. Thus, a physical modeling and good choice of boundary conditions for the unresolved vasculature is currently be preferred. The microvasculature consists of three types of small vessels: arterioles, capillaries, and venules, and the computational cost for flow simulation in these network is rather expensive [49, 51, 61]. However, coarsening the capillary networks can reduce the complexity and the computational cost. Reichold et al. [57] implemented such an approach in rats' cerebral microvasculature and found that an upscaled vessel could replace multiple vessels within a region. The capil-

lary bed volume was divided into sub-domains, minimizing the computational costs by a factor depending on the number of capillaries in the sub-domain. Nevertheless, this approach requires the full knowledge of the microvasculature to calculate the upscaled vessels, which as explained above, is not possible for living tissues. In Olufsen et al. [43], a structured tree was constructed as boundary condition for each arterial terminal to represent the capillary bed and the vein network. Combining both ideas, a structured tree from [43] can can be used to approximate the upscaled microvasculature proposed in [57].

A complex architecture of blood circulation makes it difficult not only to understand the mechanisms that occur at the various levels but also to assess their interdependence. According to Perdikaris et al. [49], a multiscale flow model is believed to have great potential for solving this problem. It also overcomes the resolution limitation in the image-based blood flow modeling, in which the observable vessels are linked using a physiologically realistic model. One approach to the multiscale flow model is a discrete-continuum system, where the microcirculation is defined as a porous media. Several studies using this approach have explored the blood flow simulation for the cerebral and liver microvasculature, both in humans and animals [14, 51, 58, 61]. Such proposed models use a blood flow model that couples a 1D vessel network model and a 3D Darcy continuum model, thus decreasing the computational cost significantly and allowing for full brain simulations [23].

It should be noted, however, that 0D and 1D models have lower accuracy with respect to full 3D models, especially when used to describe large vessels [8]. The simplified physics model, such as a 0D model, requires some adjustments to recover the loss of accuracy caused by modeling simplification, like vessel curvature, bifurcations, pressure drops, and vessel wall elasticity. These adjustments introduce nonlinearities into the modeling framework. In medical applications, this approach has become essential in place of or in addition to, fully-resolved CFD modeling [8, 40]. It results in a framework that is significantly easier to solve than existing 3D models and yet it allows for good description of changes in hemodynamics even in complex blood circulation scenarios [37]. However, only a limited number of multiscale models integrate these nonlinearities. For instance, Rohan et.al's work only incorporated pressure drop at junctions in their model, using Bernoulli's equation [58].

The application of blood flow modeling in this thesis is primarily for the development of digital reference objects in perfusion imaging MRI, such as dynamic contrast enhanced (DCE)-MRI and Arterial Spin Labeling (ASL). This imaging technique have been widely used to obtain physiological parameters for patient diagnosis, prognosis, and monitoring [13, 17, 22, 29]. The tissue parameters (e.g. plasma flow, blood volume) from imaging

data are mostly extracted by using black-box tracer-kinetic models (TKMs) [63, 66], which have systematic errors depending on the model assumptions [11, 32]. Hence, the estimation methods require evaluations and validations to provide a reliable result.

A phantom model is an artificial physical object that is scanned to test, analyze, and tune MRI systems, as well as imaging performance and quantification methods, including tracer kinetic models [72]. Digital phantoms, on the other hands, are usually constructed by using a TKM to generate synthetic data [13, 22, 36, 62]. However, this approach has the issue of model bias for evaluating TKMs since the data synthesis and the model evaluation stages are not independent. Advances in computational resources and approaches for blood flow modeling enable vast applications in the medical study [46, 49, 55, 56], including development of digital phantom in perfusion imaging.

Developing a new multiscale flow model for blood circulation and perfusion can be a daunting task due to the reasons stated above. This thesis addresses some of these issues by focusing on three major issues: i) The need for a robust and efficient framework for vasculature-induced nonlinearities in the blood circulation. ii) The complex processes occurring in microcirculation and the coupling with macrocirculation, involving meticulous physical modeling. iii) The evaluation of the framework for digital reference objects in perfusion imaging.

Given this context, a multiscale framework is introduced for blood circulation and extended to nonlinear problems in the vasculature. The framework allows a complicated problem to be divided into manageable parts by considering the individual scale domains separately, and thereby facilitates a consistent modeling and coupling between different scales of the domain. For microcirculation, two approaches are presented: a porous media in the discrete-continuum system and a direct connection model. Finally, the frameworks were used to generate synthetic perfusion imaging data for the validation of tracer kinetic models.

1.1 Main contributions

A mathematical model for multiscale structure in blood circulation that includes vasculature nonlinearities. A discrete-continuum blood flow model [23] is extended to cover vasculature nonlinearities in vessels in Paper A. The model, which is validated by using frog experimental data from [4, 35], accounts for physical processes such as elasticity and vessel bifurcation in a frog tongue blood circulation. In the vessel occlusion scenario, the nonlinear effects in the discrete-continuum system are investigated in comparison to the fully linearized model, which provides a more realistic result than the simplified model.

A direct connection model for the unobservable microcirculation. A realistic model for a continuum approach by using porous media requires a suitable permeability, which is difficult to obtain from clinical data. The homogeneous assumption allows blood to spread from an artery terminal to the entire organ, whereas blood perfusion takes place locally in the capillary bed. In Paper C, we combined Reichold et al.'s upscaled vessel concept [57] with a structured fractal tree to link the observable arteries and veins to enable us to set up an upscale pressure drop that represents the capillary network [18]. This discrete approach not only ensures local perfusion in the capillaries, but also serves as a starting point for the continuum model's permeability distribution.

Digital reference objects for perfusion imaging. Aside from providing knowledge on hemodynamics and vasculature, advancements in blood flow modeling will continue to improve a generation of various synthetic medical imaging data [3, 41, 48, 52]. The blood flow model was used to generate synthetic data that can be used to test and validate pharmacokinetic quantification methods. This application shows how a blood flow model can be used as a digital reference object for a perfusion image with controlled parameters. Paper B describes the preliminary work for generating tracer indicator flow by using the hybrid flow model. Furthermore, paper C compares and evaluates four TKMs by using a network flow model that generates synthetic data.

A study of the optimal vasculature in an organ based on multiscale flow model. The human vascular structure in nature is believed to be an optimized construction for blood circulation. A mathematical model that describes and mimics this vasculature allows for various application. By employing the multiscale framework described in Paper A, the optimization on the structure of the vascular network as the macrocirculation is studied in paper D. The fluxes and time-of-flight in the capillary bed tissue of the model were used as the basis for optimization. We discovered several local minima and a'short-cut' in generated vessels as a result of the flux optimizations. The TOF optimization results, on the other hand, were consistent and provided less stagnation in the domain, favoring better distribution of oxygenated blood and nutrients to the tissue.

1.2 Outline

This thesis is divided into two parts. Part I is an introduction to the physiological models, tracer kinetic analysis, mathematical formulations, and numerical methods used in the papers. Part II consists of one paper published in a scientific journal, one peer reviewed book chapter, and two journal articles ready for submission. The remainder of Part I is organized as follows:

Chapter 2 presents a brief overview of the physiological background theory behind the mathematical model, where the main focus is on the multiscale architecture of the blood circulation.

Chapter 3 discusses the tracer kinetic analysis of perfusion MRI.

Chapter 4 describes the mathematical model, including governing equations for fluid and tracer flow for the multiscale models.

Chapter 5 introduces the discretizations of the mathematical models stated in Chapter 4 and the numerical implementation.

Chapter 6 provides a summary of each of the papers in Part II and their scientific contributions.

Chapter 2

Physiological theory of blood circulation

In this chapter, we introduced basic concepts describing the physiology of blood flow and the fundamental theory for developing a mathematical model. The role of the blood circulation is to distribute nutrients and oxygen to the tissue, and to carry the metabolic waste away from the tissue. The oxygenated blood is pumped from heart, circulated through arteries, distributed to the tissue via capillaries. The deoxygenated blood and metabolic waste are transported away from the tissues to the heart via veins.

This chapter begins with an explanation of multiple-scale geometry and blood circulation-related notation. The model scales are separated according to the imaging modality's resolution limitation. Then the physiological aspects are discussed, such as the vascular network structure, vessel wall structure, and blood rheology.

2.1 Blood circulation system: a multiple-scale architecture

We classify the structural organization of the entire vasculature, the scales of interest and the term that will be used in the remainder of this thesis, which is shown in Figure 2.1. This classification is a simplified version from definition in Quarteroni's work [55], and similar with the hybrid models in a multiple-scale architecture in blood circulation [15, 23, 51, 61].

2.1.1 Macrocirculation

The macrocirculation is the observable vessels from an image modality (e.g. MRI, ASL, etc), typically for vasculature greater than 250 µm in diameter, and possibly up to 140 µm using a 7T whole body scanner [67] of a formalin-fixed human tissue. This vessel support a fast, stable and resilient flow. While the artery networks supply the oxygenated blood and nutrients to the organ tissue, a similar vein networks usually parallel to the

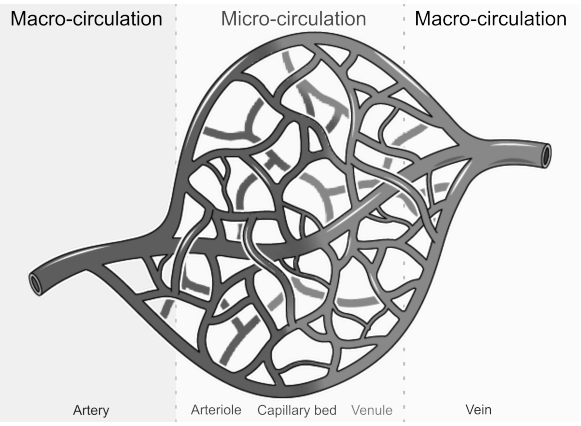

Figure 2.1: The architecture of blood circulation in this thesis consists of macro- and microcirculation. The macrovasculature is extracted from an imaging data. While the microcirculation represents the connection between the observable arteries and veins. The image was taken and edited from www. britannica. com

arteries will carry the metabolic waste contained in the blood back to the heart.

Within this study, we will focus on the macrocirculation of an organ with vessels radius below one mm and has dampened pulse wave in the upstream arterial vessels [14, 51]. Hence, the blood flow can be considered as a laminar flow.

2.1.2 Microcirculation

In connection between the arterial and vein network, we define the unobservable vasculature including arterioles, capillaries, and venules as a microcirculation. An arteriole is a small vessel that branches out from an artery and connects to capillaries. The capillaries are the smallest blood vessels in the body (5-10 µm in diameter), which form a dense interconnected vessel network known as "capillary bed". Molecular exchanges between the blood and tissue cells occurred within the capillary bed, where the red blood cells and the molecules transported by the plasma carry oxygen and nutrients. The space-filling structure of the capillary bed ensures the supplies to the whole organ regions by minimizing the distance between any point of the tissue and the capillary vessel, which involves a huge number of vessels.

Both a continuum and a discrete approach to microcirculation were employed in the thesis. The unobservable vessel networks were assumed to be porous media in the continuum method. The microcirculation can also be described as a multi-compartment system, with paper A implementing a two-compartment system for the arterial and venous capillary bed, respectively. The discrete approach describes a direct link between two adjacent artery and vein terminals within an effective radius, obviating the need for a capillary network between those terminals. This method ensures local perfusion within an effective range, which was not possible with a porous media in Paper B.

2.2 Vascular network structure

The term "vascular networks" in this study refers to the macrocirculation of an organ's vascular system, which includes artery and vein networks. One of the most noticeable geometrical features of vascular networks is branching. Murray proposed the first theoretical studies on the structure of vascular networks in 1926, employing the principle of minimum work [38, 39]. Half decade later, Kamiya and Togawa [30], and Zamir [74] proposed the principle of minimum total drag force (shear stress) on the vessel wall.

The branching vessel (child) rule was generalized by Uylings, and the radii were characterized using a scaling law with a bifurcation exponent in the range of $2 \leq \xi \leq 3$ [70]. An exponent between 2 and 2.3 corresponds to turbulent flow in the aorta, while 3 is for laminar flow in the arterioles and capillaries. This exponent value has been validated using measurement from vascular network in organs of human and animals [25–27, 31, 42, 59, 68, 69, 75, 76]. In addition, Murray defined the optimal bifurcation angle between parent and child vessel to obtain the optimal branching structure [39].

2.3 Blood vessel wall structure

The blood vessel wall is composed of three layers, each of which serves a distinct function. The inner layer is made of endothelial tissue, which allows blood to flow smoothly and without friction also acting as a sensor for wall shear stress. The middle layer is made up of smooth and elastic muscle cells that allow blood vessels to adjust the size of their lumens. Finally, the outer layer is composed of collagen, which protects, strengthens, and connect the blood vessels to the surrounding tissues.

As a result, each blood vessel has a distinct structure based on its function. Arteries have a thick layer of muscle cells and a flexible structure since they control blood flow at high pressure. Veins have a thicker outer layer and thinner walls than arteries since the lower blood pressure passing through them, despite having valves that ensure one-way blood flow. Capillaries, on the other hand, have very thin walls and no smooth muscle cells because they exchange gases and nutrients from blood vessels to surrounding tissue at low pressure.

Therefore, the mathematical model must include a specific vessel wall structure for each blood vessel to model the entire calculation. The inner wall is present in all blood vessels, but the thickness of the middle and outer wall layers vary. Because our model considers the dynamics of the vessel wall, only elasticity is used to differentiate the vessel wall structure for each vessel.

2.4 Blood rheology

Our model's main object is blood, which consists of plasma, red blood cells (erythrocytes), white blood cells (leukocytes), and platelets. Plasma is a pale yellow fluid made of proteins and electrolytes that transports cells and proteins throughout the body and accounts for approximately 55% of total blood volume. Red blood cells (RBCs) account for approximately 45 % of total blood volume (in humans), and this will be the hematocrit H_D assumption for the remainder of the thesis. White blood cells are responsible for protecting the body from infection. Platelets are blood components that aid in the blood clotting process. The last two blood components account for a much smaller proportion of total blood than RBCs, which is about 1% of total blood.

Blood plasma, which consists mostly of water, can be considered to be very close to a Newtonian fluid. The whole blood, on the other hand, has complex mechanical properties that become especially important when the particle (especially RBCs) size is comparable to the blood vessel size [53, 60]. In this case, blood cannot be modelled as a homogeneous fluid in the microcirculation, it is necessary to consider it as a suspension of blood cells in plasma. The presence of blood cellular elements and their interactions causes significant changes in blood rheological properties. Therefore, accurate measurements are required to develop appropriate a microcirculation model. Otherwise, based on the size of the blood vessels and the flow behavior, it can be classified as a Newtonian or nonNewtonian fluid.

Chapter 3

Tracer kinetic analysis

One of the goal for developing mathematical models in this thesis is to contribute to the difficult task of validating tracer kinetic models in medical applications. In this chapter we describe tracer kinetic analysis and tracer kinetic models. The main reference for this chapter is from Sourbron et. al's study [66], and we adopt much of the notation from there.

3.1 Basic theory of tracer kinetic models

A *tracer* is an indicator molecule that follows a systemic substance, such as blood, within a system or an organ [73]. Tracing these systemic substances in a system, that is, analyzing their temporal and spatial distributions, contributes important informations about the substance kinetics and the metabolic functioning of the system itself. The conservation of tracer mass serves as the foundation for all tracer kinetic models. In addition, the general tracer kinetic theory of linear and stationary systems is the foundation for understanding them [50, 64, 66].

3.1.1 Conservation of tracer mass

Consider a region of tissue has several inlets and outlets, which a tracer may be delivered to one or more of these inlets. The *tissue tracer concentration* $C(t)$ [M] is a value measured directly in MRI, namely the number of tracer molecules relative to the total volume of tissue. The tracer's *volume of distribution* v (dimensionless or in [ml/100ml]) is the volume fraction of tissue that is accessible to the tracer, i.e. intravascular and interstitium space, which is equivalent to the porosity of tissue. Since the tracer is a water-soluble substance, it is restricted in the blood plasma, and the volume of distribution for whole blood therefore depends on the hematocrit, H_D:

$$v = v_b \left(1 - H_D\right), \tag{3.1}$$

where v_b denotes the total blood volume. The *blood tracer concentration* $c(t)$ [M] is defined as the number of tracer molecules in blood relative to the volume of distribution:

$$c(t) = \frac{C(t)}{v}. \tag{3.2}$$

The blood flow in the inlet or outlet is defined as the tracer *clearance* F (in [ml/min/100ml] or [min^{-1}]) that is normalized to tissue volume [50]. The tracer *flux* $J(t)$ [mol/min/ml] is the number of tracer molecules through an inlet or outlet per minute:

$$J(t) = Fc(t). \tag{3.3}$$

The rate of change of the tissue concentration is equal to the difference between the total influx and outflux in a region of tissue:

$$\frac{dC(t)}{dt} = \sum_{i \in \text{Inlets}} F_i c_i(t) - \sum_{o \in \text{Outlets}} F_o c_o(t), \tag{3.4}$$

where $c_i(t)$ and $c_o(t)$ represent the tracer concentration at each inlet and outlet, respectively. Equation (3.4) is the conservation of tracer mass inside a tissue region.

3.1.2 Linear and stationary systems

A relation between influx and outflux in a tissue region can be obtained through the notion of *tracer transit time*, defined as the time elapsed between entering and leaving the tissue. Because of the probabilistic nature of particle movement in tissue, the tracer passage for inlet i is characterized by a probability distribution of transit times $H_i(t)$ [min^{-1}]. If we assume the response to an influx is proportional to the concentration (linear) and $H_i(t)$ is independent of the time of injection (stationary), the inlet i contributes to the total outflux out of the tissue as follows:

$$\sum_{o \in \text{Outlets}} J_o(t) = \sum_{i \in \text{Inlets}} H_i(t) * J_i(t), \tag{3.5}$$

where the convolution product * of two function $f(t)$ and $g(t)$ is defined as follows:

$$f(t) * g(t) = \int_0^t dx f(x) g(t - x). \tag{3.6}$$

Inserting equation (3.5) into equation (3.4) and integrating the result produces a relation between tissue concentration and influx:

$$C(t) = \sum_{i \in \text{Inlets}} Res_i(t) * J_i(t), \tag{3.7}$$

The residue function $Res_i(t)$ of the inlet i is the fraction with a transit time larger than t, defined in terms of $H_i(t)$:

$$Res_i(t) = 1 - \int_0^t H_i(u)du \quad \text{or} \quad H_i(t) = -\frac{dRes_i(t)}{dt}. \tag{3.8}$$

Another implication is that the *mean transit time*, T [min], is equal to the area under curve $Res(t)$:

$$T = \int_0^\infty Res(t)dt. \tag{3.9}$$

In general, the measured tissue concentration $C(t)$ and the arterial influx concentration $c_a(t)$, known as arterial input function (AIF), are related by convolution with an impulse response function $I(t)$(insert equation (3.3) into (3.7) with a single inlet):

$$C(t) = I(t) * c_a(t) \quad \text{with} \quad I(t) = F_p Res(t). \tag{3.10}$$

This function be determined by the tissue characteristic model assumption and parameters in TKM that will be discussed further in the following section.

3.2 Compartment models

A compartment is defined as a well-mixed space, i.e. a region where the concentration is spatially uniform within the volume of distribution. As a consequence, the concentration at any outlet must equal the uniform tissue concentration $c(t)$. The equation of mass conservation(3.4) for a compartment then depends on $c(t)$ and the inlet concentrations, $c_i(t)$ (inserting equations (3.2) into (3.4)):

$$v\frac{dc(t)}{dt} = \sum_{i \in \text{Inlets}} F_i c_i(t) - \sum_{o \in \text{Outlets}} F_o c(t). \tag{3.11}$$

Solving this equation for $c(t)$ and comparing the result to equation (3.7) shows that a compartment is characterized by an exponential decaying residue function:

$$Res(t) = e^{-t/T} \quad \text{with} \quad T = \frac{v}{\sum_{o \in \text{Outlets}} F_o}. \tag{3.12}$$

In equation (3.9), the area under curve $Res(t)$ can represent the mean transit time of the compartment. This result show that T depends only on the volume of distribution and the total outlet clearance, and independent of the inlet.

A multi-compartments model compromises of n interconnected compartments, where the inlets of one compartment is the outlets of another. Applying equation (3.11) to each compartment accordingly produces a system of n first-order differential equations [34, 66].

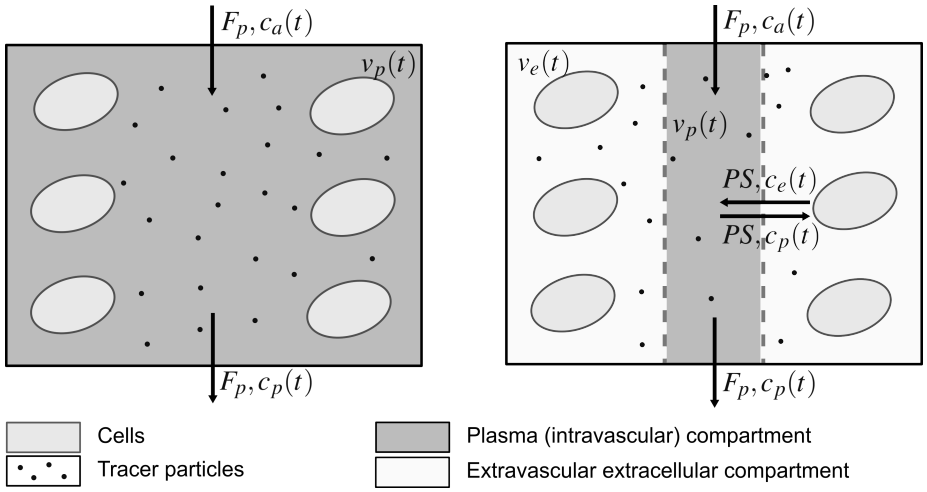

Figure 3.1: Schematic illustration of a simplified model of the capillary-tissue system in the one- and two-compartment model. The plasma flow F_p carries tracer particles into and out of the tissue of interest. The compartment assumption causes the tracer concentration flow rate proportional to the upstream compartment concentration. (Left) The one-compartment model consider the whole extracellular space as a single plasma compartment. (Right) Plasma and interstitium are defined as compartments in the two-compartment model, the interstitium can only exchange with the plasma compartment at a rate determined by PS.

3.3 Tracer kinetic models

The thesis will focus on the models that are most commonly applied for extracting blood flow F_p and blood volume v_p parameters from DCE-MRI imaging data. The models below are fundamentally based on the compartment model for the capillary tissue [20, 28, 32, 34, 66]. Figure 3.1 shows the illustration of the one- and two-compartment models.

3.3.1 One-compartment model (1CM)

The one-compartment model describes a tissue consisting of a single well-mixed 'extracellular' compartment to represent the plasma space (with plasma's volume of distribution v_p) inside a tissue region. The mass balance for a capillary compartment is:

$$v_p \frac{dc_p(t)}{dt} = F_p \left[c_a(t) - c_p(t)\right], \tag{3.13}$$

where F_p is the plasma flow and c_p is the plasma concentration. The solution for this model is

$$Res(t) = e^{-t/T_p} \quad \text{with} \quad T_p = \frac{v_p}{F_p}, \tag{3.14}$$

yields an impulse function

$$I(t) = F_p e^{-t\frac{F_p}{v_p}} \tag{3.15}$$

and inserting this into equation (3.10) gives

$$C(t) = F_p e^{-t\frac{F_p}{v_p}} * c_a(t). \tag{3.16}$$

3.3.2 Maximum slope model (MS)

The maximum slope model is a no-outflux model, by assuming no indicator molecule leaving the tissue region when the indicator influx rate reaches the maximum value. This model is based on a single-compartment with a simplified conservation of indicator mass as follows (equation (3.13)):

$$\frac{dC(t)}{dt} = F_a c_a(t) - F_v c_v(t), \tag{3.17}$$

where indexes a and v denote the arterial inlet and the vein outlet, respectively. In an enclosed tissue region, the inlets and outlets indicator clearance will be equal, $F_a = F_v = F_0$:

$$\frac{dC(t)}{dt} = F_0 \left[c_a(t) - c_v(t)\right]. \tag{3.18}$$

If t is much smaller than the indicator transit time in the tissue ($t \ll T_p$), then we can assume that $c_v(t) \approx 0$ when $c_a(t)$ reaches maximum value. Therefore, it holds that

$$F_0 = \frac{\max_t C'(t)}{\max_t c_a(t)}, \tag{3.19}$$

where the tissue concentration rate $C'(t)$ will be maximized if $c_a(t)$ is maximum since the system is stationary.

3.3.3 Two-compartment exchange model (2CXM)

The Two-compartment exchange model describes two compartments, 'plasma' (v_p) and 'interstitial volume' (v_e), with their exchange in terms of capillary permeability PS in addition to F_p (see the schematic illustration in Fig. 3.1). The indicator mass balance for a plasma compartment has the form of equation (3.13) with an additional the interstitium parameter:

$$v_p \frac{dc_p(t)}{dt} = F_p c_a(t) - F_p c_p(t) + PS c_e(t) - PS c_p(t), \tag{3.20}$$

and mass conservation for interstitium compartment:

$$v_e \frac{dc_e(t)}{dt} = PS c_p(t) - PS c_e(t), \tag{3.21}$$

where the total tissue concentration $C(t)$ is defined as

$$C(t) = v_p c_p(t) + v_e c_e(t). \tag{3.22}$$

Solving equation (3.20), (3.21) and (3.2) yields the impulse function for 2CXM, which is given by

$$I(t) = Ae^{x_1 t} + (1 - A)e^{x_2 t}, \tag{3.23}$$

where the exponents are roots of a quadratic equation [12, 34, 65]

$$x_1, x_2 = \frac{1}{2}\left[-\left(\frac{PS + F_p}{v_p} + \frac{PS}{v_e}\right) \pm \sqrt{\left(\frac{PS + F_p}{v_p} + \frac{PS}{v_e}\right)^2 - 4\frac{PS}{v_e}\frac{F_p}{v_p}} \right], \tag{3.24}$$

and the coefficients are

$$A = \frac{\alpha + \frac{PS}{v_p} + \frac{PS}{v_e}}{\alpha - \beta} \quad \text{and} \quad (1 - A) = \frac{\beta + \frac{PS}{v_p} + \frac{PS}{v_e}}{\beta - \alpha}. \tag{3.25}$$

3.3.4 Two-compartment uptake model

The 2CUM is a simplified version of the 2CXM, by assuming a long mean transit time (MTT) compared to measurement time, hence, there is only uptake flow from v_p to v_e during measurement time [12, 65]. Hence, the backflux $PSc_e(t)$ from interstitium in the 2CXM will be neglected (equation (3.20) and (3.21)), result in a conservation of mass for plasma compartment:

$$v_p \frac{dc_p(t)}{dt} = F_p c_a(t) - F_p c_p(t) - PSc_p(t), \tag{3.26}$$

and for interstitium compartment:

$$v_e \frac{dc_e(t)}{dt} = PSc_p(t). \tag{3.27}$$

Solving the equations (3.26) and (3.27) yields the residue function for each compartment

$$Res_p(t) = e^{-t/T_p}, \tag{3.28}$$

$$Res_e(t) = E_F(1 - e^{-t/T_p}), \tag{3.29}$$

where

$$T_p = \frac{v_p}{F_p + PS} \quad \text{and} \quad E_F = \frac{PS}{F_p + PS} \tag{3.30}$$

are the mean transit time in the plasma compartment and the exchange fraction, respectively. The impulse function for the two-compartment uptake model is given by $I(t) = F_p[R_p(t) + R_e(t)]$, inserting this function to equation (3.10) yields

$$C(t) = F_p\left[(1 - E_F)e^{-t/T_p} + E_F\right] * c_a(t). \tag{3.31}$$

3.4 Delay and dispersion

The above described system is assuming AIF, in the tissue region is measured directly at each inlet. In practice, the tracer concentration is measured in a bigger upstream vessel, so that the actual inlet concentration is both delayed and dispersed compared to the measured upstream AIF. A delay can be detected in a poor fit in the upslope of the first pass and easily be fixed by shifting the impulse function according to the time delay

$$I(t) = F_p R(t - T_0). \tag{3.32}$$

T_0 represents time delay, an additional parameter that can be determined by a suitable model fitting procedure [5]. While dispersion can only be corrected by modelling the vascular tracer transport explicitly [6, 7]. The correction is implemented by a convolution of vascular transit time $H_a(t)$ into the impulse function (equation (3.10)):

$$I(t) = F_p R(t) * H_a(t), \quad \text{with} \quad H_a(t) = \frac{e^{-t/T_a}}{T_a}, \tag{3.33}$$

where T_a denotes the mean arterial transit time, i.e. the average time required for tracer to travel from AIF measured location to the local inlet at the region of interest (ROI). This value may be estimated using computational fluid model, such that the local AIF can be computed from the measured AIF. In general, the combination of delay and dispersion can be expressed by

$$H_a(t) = \frac{e^{-t/T'_a}}{T'_a} * \delta(t - T''_a), \tag{3.34}$$

where T'_a and T''_a are the dispersion time and delay time, respectively. The sum of both values is the mean transit time of the arterial vasculature, $T_a = T'_a + T''_a$.

Chapter 4

Mathematical model for blood circulation

The physiological theory of blood circulation has been introduced in Chapter 2 and is the starting point for developing the mathematics and geometry applicable to the model scale. Before going deeper into the flow model, the first section describes the simplifications and hypotheses for blood flow. The rest of this chapter is organized as follows. First, we define the geometry for multi-scale modeling, as well as the modeling objects and notation used to label them. The mathematical model for each scale is then described, including the model connection via coupling and the boundary conditions. Finally, the transport equation for tracer flow modeling in the blood circulation is introduced.

4.1 Main simplifications and hypotheses

In this thesis, the blood flow are simulated with focus on the following main assumptions:

- The segment of the blood vessel is considered as a long cylindrical tube with a constant radius and non-slip conditions on the vessel walls.
- The blood hematocrit is assumed to be uniform in the whole vasculature, so that the distribution of the red blood cells and the nonlinearities induced by it are neglected [23, 51, 57].
- The capillaries and small vessels is assumed to be isotropic and homogeneous for continuum approach in microcirculation.

We also present a number of other hypotheses that apply to all frameworks. First, blood flows at approximately 1-5 cm/s in small artery and vein vessels less than 1 mm in radius, and approximately 1 mm/s in the capillary network, so the Reynolds number is consistently less than 200, allowing inertial effects to be ignored and the flow to be

laminar. Second, because the Womersley number in small vessels is less than 0.1, the pulsatility is negligible. The flow is then assumed to be stationary. We also conclude that the mass density of blood ρ and gravity $\mathbf{g}$ are constant throughout the circulation, so the pressures used in all calculations are defined as fluid pressures minus hydrostatic pressures.

4.2 Vascular network model

A vascular network is an interconnected vessels forming either a network of artery and veins. A single vessel segment in the vascular network is constituted by Poiseuille's law and some nonlinearities induced by the vasculature. The last, several vessels connected into a vessel network model, require boundary conditions.

4.2.1 Poiseuille equation

The basis for our blood flow models is the Poiseuille equation [57, 61]. This is the simplified Navier–Stokes equation for an incompressible Newtonian fluid flow with pressure gradient as the only driving force.

$$\frac{\partial \mathbf{u}}{\partial t} + (\mathbf{u}.\nabla)\mathbf{u} = -\frac{\mu}{\rho}\nabla^2\mathbf{u} - \frac{1}{\rho}\nabla P + \mathbf{f}, \tag{4.1}$$

where $\mathbf{u}$ is the velocity field, and the fluid has viscosity μ and density ρ; the fluid flow driving force are a pressure field P and a body force $\mathbf{f}$ (which is assumed to be zero). If the flow is assumed to be steady and the advection term is neglected, then this reduces to

$$0 = -\frac{\mu}{\rho}\nabla^2\mathbf{u} - \frac{1}{\rho}\nabla P.$$

If the vessel is then assumed to be a long cylindrical tube, so that we can assume a purely axial flow (i.e. with negligible radial and circumferential velocity components), then this further reduces to

$$0 = -\frac{\mu}{\rho r}\frac{\partial}{\partial r}\left[r\frac{\partial u_z}{\partial r}\right] - \frac{1}{\rho}\frac{\partial P}{\partial z} \tag{4.2}$$

with the subscript z is the axial component of flow and it is assumed that the pressure is uniform over the cross-sectional area.

We can solve equation (4.2) with no slip boundary condition that requires $u_z = 0$ at the vessel wall and symmetry at the flow center-line. Integrating the solution over the vessel volume of length L and radius r give the flow resistance in the vessel, which known as hydraulic resistance

$$R = \frac{8\mu L}{\pi r^4}, \tag{4.3}$$

with

$$\Delta P = QR, \tag{4.4}$$

where ΔP denotes the applied pressure difference and Q is the volumetric blood flow in the vessel. This relationship is equivalent to the Ohm's law in electrical circuit that is one of the basic concept in a lumped parameter model [44, 45, 55].

4.2.2 Blood viscosity in the microvasculature

In the Poiseuille equation (4.3), the resistance to flow is linearly proportional to the viscosity of blood. The viscosity is only a function of the blood haematocrit in larger vessels, but in small vessels it is also strongly dependent upon the vessel diameter. This is due to the finite size of red blood cells, typically around 8μm, is in the same order of magnitude as that of the diameters of the smaller blood vessels; and the interaction between these cells and the vessel wall which it is flowing results in a number of interesting types of behaviour. This is known as the Fåhraeus-Lindqvist effect and may be accounted for by letting the viscosity depend on the vessel radius. Experimental studies show a decreased apparent viscosity in vessels with a diameter from 300μm to about 10μm [60]. Therefore, the capillaries with diameter in this range contribute significantly to the total resistance in the vascular system. We use the algebraic relationship of Secomb and Pries's work to describe radius-dependent viscosity [60],

$$\mu(d) = \mu_0 \left[1 + (\mu_{0.45} - 1)\frac{(1 - H_D)^G - 1}{(1 - 0.45)^C - 1}\left(\frac{d}{d - 1.1}\right)^2\right]\left(\frac{d}{d - 1.1}\right)^2 \tag{4.5}$$

where μ_0 is the normal blood viscosity, $d = 2r$ is the vessel diameter, H_D is the blood hematocrit with $H_D = 0.45$ for reference,

$$\mu_{0.45} = 6\exp(-0.085d) + 3.2 - 2.44\exp(-0.06d^{0.645}) \tag{4.6}$$

and

$$G = (0.8 + \exp(-0.075d))(-1 + (1 + 10^{-11}d^{12}) - 1) + (1 + 10^{-11}d^{12})^{-1}. \tag{4.7}$$

Introducing equation (4.5) into the whole vascular system allows to determine the blood viscosity for each vessel, and maintain the linearity of the Poiseuille equation (4.3).

4.2.3 Vessel wall model

Vessel wall elasticity is a physiological regulatory factor that forces blood flow in a particular direction. On the other hand, the vessel wall elasticity also allows for a vessel radius dependence on the pressure gradient, to favour blood supply in case of

an alteration of the vascular system [71]. The vessel wall has stiffness G at a baseline pressure P_0 and the vessel area A_0 during normal (rest) condition is given by the Young's modulus and Poisson's ratio of the linear elastic material as follows

$$G = \left.\frac{dP}{d(A/A_0)}\right|_{A=A_0} = \frac{h_0}{r_0}\frac{E}{2(1-\lambda^2)}, \tag{4.8}$$

where h_0 is the vessel wall thickness, E is the Young modulus, r_0 is the initial vessel radius during rest, and λ is the Poisson ratio. The pressure drop due to a change in radius is described by the independent ring model [16] that neglects shear stress and longitudinal displacement of vessel:

$$\Delta P = P - P_0 = 2G\left[\sqrt{\left(\frac{A}{A_0}\right)} - 1\right], \tag{4.9}$$

where P_0 and A_0 are a baseline pressure and the vessel area during normal (rest) condition. Whereas P and A are the pressure and vessel area during compression or expansion, respectively. The pressure P is defined as an average pressure in the vessel segment, which is simplified as the average pressures at both vessel endpoints. The elasticity equation (4.9) has the effect of introducing a nonlinearity to equations (4.4).

4.2.4 Flow in a vascular network

In this section, we show how the above models presented for blood flow in single vessels can be combined into a model for a vascular network. First, the flow is considered to be in steady state, the Poiseuille equation (4.3) can be assumed. Then the viscosity of the fluid needs to be known for each vessel. If a constant hematocrit is used, then the resistance can be calculated as a function solely of the radius, Eq. (4.5). If the vessel is also considered elastic, then the elasticity (4.9) is included into the system.

The remaining assumption that needs to be made is how the boundary conditions for each vessel are linked together. Conservation of flow is needed and however there are two different approaches that are used to match pressure at nodes. 1) The static pressure at the node is equal at the end of each connecting vessel and independent to the flow rate in vessels, which is the more common assumption and leads to the most straightforward mathematical model. 2) The total dynamic pressure at the exit of a vessel is matched at the inlet to all connected vessels:

$$P_0 + \frac{1}{2}\rho u_0^2 = P_1 + \frac{1}{2}\rho u_1^2 = P_2 + \frac{1}{2}\rho u_2^2, \tag{4.10}$$

where indexes 0, 1 and 2 denote each connected vessel at a junction. Both methods are widely used, although little formal consideration has been given to the differences.

In this thesis, a total pressure match scheme was used to define vessel pressure drop connected to the junction node, which also allows for energy loss at bifurcation [40, 47]. An additional pressure drop estimation was defined from [8],

$$\Delta P_n^b = \frac{\rho Q_{dat}^2}{2\pi^2 r_{dat}^4}\left(1 + \frac{Q_n^2 r_{dat}^4}{Q_{dat}^2 r_n^4} - \frac{2Q_n r_{dat}^2}{Q_{dat} r_n^2}\cos\left(\frac{3}{4}\theta_{(dat,n)}\right)\right), \tag{4.11}$$

where the upper index b stands for bifurcation and the index dat refer to the *datum* vessel, i.e. the vessel from which the flow approaches the junction. Further, $\theta_{(dat,n)}$ is the angle between the datum vessel and vessel n. The pressure drop equation was constructed based on Bernoulli equation to match the total pressure at the inlet and outlet vessels at bifurcation. The derivation details were described on Mynard et al.'s work for converging and diverging flow at a junction [40]. Hence, the total pressure drop after a bifurcation node was computed as the sum of both equation (4.4) and (4.11),

$$\Delta P_n = \Delta P_n^h + \Delta P_n^b. \tag{4.12}$$

In addition to flow conservation, the model must have Dirichlet boundary conditions at the vascular network's inlet and outlet, which can be either pressure or volumetric flow.

4.3 Porous medium model

The hybrid model is an upscale approach for blood flow modelling in the multiscale architecture of blood circulation [16, 51, 55]. This model combines the vascular network model for the macrocirculation and a porous media as the microcirculation. The flow in the unobservable vessels are defined using Darcy's single-phase flow equation and discretized with a uniform grid. The complex network of small vessels and capillaries are simplified by modeling the capillary bed with Darcy equations. As a result, it can reduce computational costs while still producing reliable blood flow results in the capillary network. The disadvantage of this method is the inhomogeneity of capillaries in organ tissue, which necessitates careful modeling to resemble the blood flow in a real capillary network. In this thesis, we assume the permeability of the capillary bed is homogeneous.

4.3.1 Conservation of mass

Conservation law, which includes mass conservation, energy conservation, and momentum conservation, serves as the foundation for many physical models' frameworks. According to the law of conservation of mass, the change in mass within a volume $K \subset \Omega_i$ equals the sum of the fluxes flowing over the volume boundary and any sources and

sinks q within the volume:

$$\int_K \frac{\partial(\phi\rho)}{\partial t} dV = -\int_{\partial K} \rho \mathbf{v} \cdot \mathbf{n} dA + \int_K q dV \tag{4.13}$$

where ϕ is the porosity of the porous media (microcirculation), $\mathbf{v}$ is the blood flow flux, and $\mathbf{n}$ is the outward pointing normal vector. In this model, q is a source or sink, for instance describing the flow in or out a terminal node in the arterial or venous system for coupling with vascular network model, or a describing the passage of flow from one compartment to the other. The conservation of mass must be valid for any volume Ω_i, hence, by the divergence theorem

$$\frac{\partial(\phi_i \rho_i)}{\partial t} + \nabla \cdot \rho_i \mathbf{v}_i = q_i. \tag{4.14}$$

4.3.2 Fluxes

In addition to the mass conservation, the constitutive laws are needed to describe the physical process of interest. The capillary bed, which blood flows through, is defined as a porous medium in this context. Darcy's law, which applies to creeping blood flow in capillaries, states that a fluid flows from regions of higher pressure to regions of lower pressure in a linear manner. Thus

$$\mathbf{v} = -\frac{\mathbf{K}}{\mu}(\nabla P - \rho \mathbf{g}), \tag{4.15}$$

where $\mathbf{v}$ is the Darcy flux (volumetric flow rate per unit area), $\mathbf{K}$ is the permeability tensor of the porous medium, μ is the viscosity [10], and $\mathbf{g}$ is the gravity acceleration. There are many common assumptions to simplify the system, which is also used in this thesis, that the blood is an incompressible fluid (ρ is constant) and neglect gravitational terms. Incorporating Darcy flow into the continuity equation (4.14) gives

$$-\nabla \cdot (\frac{\mathbf{K}}{\mu} \nabla P) = q. \tag{4.16}$$

The capillary bed is described as a dual compartment system, using one compartment for the arterial part and one for the venous part. Blood perfusion is interpreted as the interchange between the two compartments, i.e. the exchange of oxygenated blood with deoxygenated blood in the capillary bed. The driving force for perfusion is the pressure difference between the two compartments [23], giving the linear relation

$$Perf = \alpha(P_{art} - P_{vein}) \tag{4.17}$$

where α is the perfusion parameter. The Darcy model for the two compartments becomes

$$-\nabla \cdot (\frac{\mathbf{K}_\beta}{\mu} \nabla P_\beta) = q_\beta + Perf \qquad \text{in } \Omega_v \tag{4.18}$$

where $q_\beta = \frac{\rho Q_\beta}{V}$ and the index $\beta = \{art, vein\}$ stands for artery and vein respectively.

4.3.3 Boundary conditions

To complete the mathematical model of the blood flow in the porous media, the conservation of mass and governing equations must be supplemented by suitable boundary conditions. The boundary condition for each compartment Ω_i in a multi-compartment model

$$u_\beta \cdot n_\beta = 0 \quad \text{(Neumann BC)} \quad \text{on } \partial\Omega_\beta, \tag{4.19}$$

In hybrid model, both the arterial and venous Darcy systems are combined with the terminal nodes of the arterial and venous networks as point sources/sinks for porous media model (microcirculation). The analytic solution of the Darcy equation around these points is a Dirac delta function, with a singularity at the source/sink point, creating a problem at the 3D-1D interface. To avoid this problem, a fluid distribution function is introduced [23]

$$f(x) = \begin{cases} C_D \exp\left(\frac{-1}{1-|x|^2}\right) & \text{if } |x| < 1 \\ 0 & \text{if } |x| \geq 1 \end{cases} \tag{4.20}$$

and use this function with a finite radius ϵ, $f^\epsilon(x) = f(\frac{x}{\epsilon})$ on the Darcy domain. C_D is described as a quadratic function. Thus, at a terminal node l (source/sink), we take

$$q_l^\epsilon = \int_\Omega q_l(x) f^\epsilon(x - x_l) dx. \tag{4.21}$$

Beside mass continuity, we have to describe pressure continuity between the 1D vascular graph and the 3D Darcy model. The pressure drop between the terminal node i and the surrounding tissue is thus given as

$$P_l - \int_\Omega P(x) f^\epsilon(x - x_l) dx = \kappa Q_l, \tag{4.22}$$

where κ represents the resistance estimation for capillary system around terminal i in the Darcy model. The resistance is estimated by computing resistance of a cylindrical tube connecting a terminal node to the Darcy domain inside a finite radius ϵ using equation (4.3). The tube radius is computed using Murray's law in bifurcation, $r_t^3 = N_\epsilon r_c^3$, with r_t is the radius of terminal node, N_ϵ is the number of cells (discretized units in Darcy domain) inside radius ϵ, and r_c represents the tube radius. The tube length is equal to the radius ϵ.

Both flow and pressure couplings between the vascular graph and Darcy model close the loop from the arterial roots to the venous roots. While a well-posedness analysis of the full model with nonlinear effects is beyond the scope of this paper, a linearized model similar to the one considered in this model was recently shown to be well-posed, both in the continuous setting and when discretized by low-order finite volume methods [24].

4.4 Direct connection model

This section introduces a direct connection model as an upscale approach to describe microcirculation, which is essentially an interconnected vascular network consisting of capillaries, arterioles, and venules [14, 51, 56, 57]. A vascular graph model based on Poiseuille equation (4.3) is, therefore, a straightforward approach for this structure. However, it relies on computational resources and needs a fine detail of the vascular network [57]. The direct connection network models the linkage between the observable vascular network (including arterioles, veneers and capillaries of less than 30 microns) which cannot be directly observed due to the limitations in the imaging modality resolution.

4.4.1 Capillary network

We hypothesize that the flow of blood in capillaries is localized in a *connection area* close to the network terminals. Over a sufficiently short time, the microcirculation in the connection area can be interpreted as a series of major streams (direct connections) between the terminal nodes of the arterial and venous vessels feeding the area. We define the connection area as a circular (spherical in 3D) region centered at a terminal of the arterial networks with radius ρ_c, as seen in figure 4.1. The value of ρ_c can be related to the smallest resolution for vessels in perfusion MRI imaging data. We assume no flow observed between arterial or venous vessels which belong to different connection area.

A *direct connection* is an extra network vessel, linking the arterial terminal to a venous terminal in the same connection area. The pressure gradient across the connection (4.3) is multiplied by a constant, γ, the *relative capillary resistance* to account for the capillarity effect in direct connection k, yielding a pressure drop

$$P_a - P_v = \gamma \frac{8\mu L_k Q_k}{\pi r_k^4}. \tag{4.23}$$

The analytic derivation of the relative capillary resistance γ is explained below.

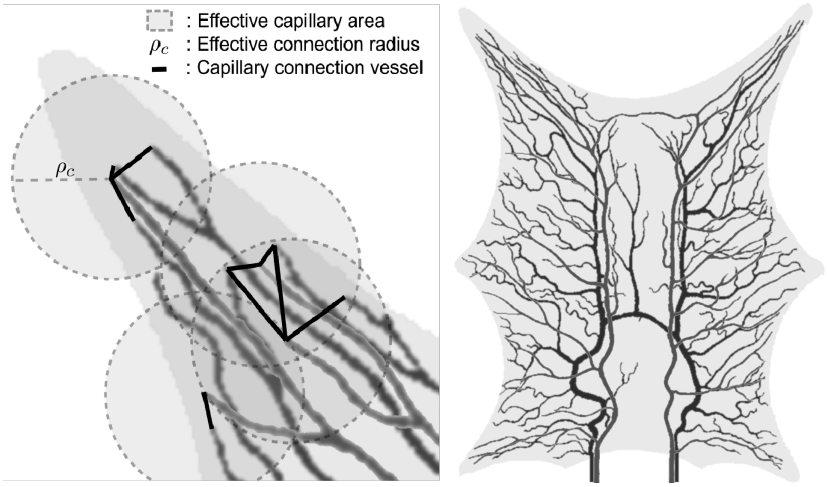

Figure 4.1: Fig. 1 of paper C, the direct connections (black lines, left image) are introduced to model unresolved vessels (including arterioles, venules and capillary tissue with a radius less than 30 microns). The flow resistance in each direct connection was analytically computed from parameters derived from the corresponding connection area (cyan circle, left image), see text for details. The vascular network structure in our simulation was obtained from the classical work [9] and extracted using the imaging segmentation process in [19]. Direct connections for the complete network structure are shown as black lines between terminal nodes, right picture).For a more detailed description of the figure, see the original figure in paper II

4.4.2 Capillary resistance relative

The parameter γ in (4.23) is determined analytically to account in the direct connection vessel for the resistance due to the flow in the connection area. This is done by extending the arterial and venous tree at the terminals with auxiliary branching, up to n-generations, and connecting the auxiliary arterial terminals to the corresponding auxiliary venous terminals (see figure 4.2). The two auxiliary networks are identical and symmetric. Direct connection k has length L_k (distance between the connected arterial and venous terminals) and radius r_k. The latter is computed using Murray's law for vessel bifurcation,

$$r_t^3 = \sum_{i \in N_c} r_i^3, \tag{4.24}$$

where r_t is the radius of arterial terminal t node, and N_c is the number of direct connections from the arterial terminal node t in the connection area. The direct connections in the same connecting area are assumed to have the same radius, thus $r_k = r_t N_c^{-1/3}$.

The length of each branch in the auxiliary trees is assumed to be proportional to the auxiliary vessel radius and subject to the constraint that the total length projection to be equal to L_k, the length of the direct connection, coinciding with the distance between the connected terminal nodes prior to the auxiliary network's construction (see figure 4.2).

$$L_k = 2(L_1 \cos\theta_1 + L_2 \cos\theta_2 + ... + L_n \cos\theta_n) \tag{4.25}$$

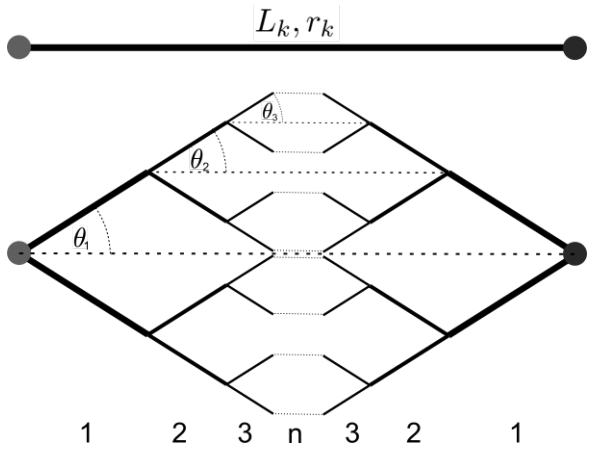

Figure 4.2: The auxiliary networks in a connection between the observable artery (red) and vein (blue) terminal nodes(top figure). The auxiliary branches are generated to n-generation represents the resistance relative in the direct connection (bottom figure).

with θ the angle between the parent vessel and the child vessel is defined as

$$\cos\theta = \frac{r_p^4 + r_{c1}^4 - r_{c2}^4}{2(r_p r_{c1})^2}, \tag{4.26}$$

where r_p is the parent vessel radius and r_{c1}, r_{c2} are the two child vessel radii [39]. Because of the symmetric branch assumption for children pairs in the auxiliary network, results $\cos\theta_n = r_{n-1}^2/2r_n^2$ and the n-generation radii is

$$r_n = 2^{(n/3)} r_k. \tag{4.27}$$

Inserting equation (4.26) into (4.25) yields

$$L_k = \frac{L_1 r_k^2}{r_1^2} + \frac{L_2 r_1^2}{r_2^2} + ... + \frac{L_n r_{n-1}^2}{r_n^2}. \tag{4.28}$$

By substituting equation (4.27), then this reduces to

$$L_k = 2^{\frac{2}{3}} \left(L_1 + L_2 + ... + L_n\right). \tag{4.29}$$

The length of vessel is assumed to be proportional to its radius, $L_n \propto r_n$. Then, the n-generation vessel length is $L_n = 2^{\frac{1-n}{3}} L_1$. So, the equation (4.29) can be written in L_1 as

$$L_k = 2^{\frac{2}{3}} L_1 \left(1 + 2^{-\frac{1}{3}} + ... + 2^{\frac{1-n}{3}}\right). \tag{4.30}$$

Due to the child vessel symmetric has similar resistance, the pressure drop in each generation vessels are identical. It therefore satisfies the parallel circuit rule in electrical, which follows the hypothesis in a 0D/lumped parameter blood flow modelling [43]. The

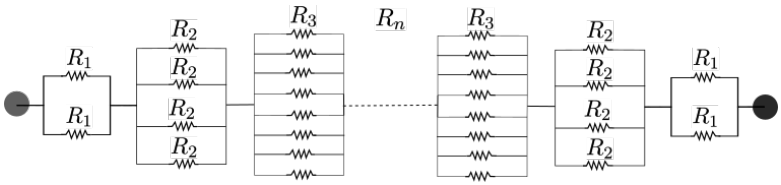

Figure 4.3: An electric circuit scheme representation of the structured tree represents the calculation of the equal resistance replacement for the whole system.

equivalent resistance simplifies the whole networks as for resistors in an electrical circuit. The electric circuit representation is described in figure 4.3,

$$R = R_1 + \frac{R_2}{2} + \frac{R_3}{4} + ... + \frac{R_n}{2^{(n-1)}}. \tag{4.31}$$

Each vessel in n-generation has resistance computed using Poiseuille equation (4.3). Hence, the total resistance in the structured tree

$$R = \frac{8\mu}{\pi}\left(\frac{L_1}{r_1^4} + \frac{L_2}{2r_2^4} + \frac{L_3}{4r_3^4} + ... + \frac{L_n}{2^{(n-1)}r_n^4}\right). \tag{4.32}$$

By substituting equation (4.30) and (4.27), the resistance in the structured tree is

$$R = \frac{8\mu L_k}{\pi r_k^4}\left(\frac{2^{\frac{2}{3}} + 2^{\frac{5}{3}} + ... + 2^{\frac{3n-1}{3}}}{1 + 2^{-\frac{1}{3}} + ... + 2^{\frac{1-n}{3}}}\right). \tag{4.33}$$

The effective resistance of the auxiliary branching with n generations is then given analytically by

$$\gamma_n = \frac{\sum_{i=1}^{n} 2^{(3i-1)/3}}{\sum_{i=1}^{n} 2^{(1-i)/3}} \tag{4.34}$$

This leaves us with a decision on the number of generations n for the auxiliary trees. One alternative is to define a minimum radius, $r_n = r_{min}$ [44]. In the current analysis, we use $n = 1$ for simplicity's sake ($\gamma = \gamma_1$). Further analysis and comparative findings for different values of n are beyond the scope of this work.

The resistance will have the radius dependent viscosity for each vessel in the auxiliary networks when including the Fåhraeus-Lindqvist effect (equation (4.5)),

$$R = \frac{8L_k}{\pi r_k^4}\left(\frac{\sum_{i=1}^{n} \mu(2^{-i/3}r_k)2^{(3i-1)/3}}{\sum_{i=1}^{n} 2^{(1-i)/3}}\right), \tag{4.35}$$

Thus, the flow resistance (4.23) in the direct connection has radius dependant viscosity as this effect is apparent in vessels with radii up to 300 μm. Combined with equation (4.34) we get

$$R_n = \frac{8L_k}{\pi r_k^4}\left(\frac{\sum_{i=1}^{n} \mu(2^{-i/3}r_k)2^{(3i-1)/3}}{\sum_{i=1}^{n} 2^{(1-i)/3}}\right) \tag{4.36}$$

with index k refers to the connecting vessel. To maintain the linearity of the system, the viscosities of each vessels were computed before solving the system.

3D auxiliary structure

The direct connection model is not only limited to the 2D structure but also allows for a 3D vascular system with a simple alteration. Rotating the branch for each generation with an axis parallel to the connection vessel (dashed line in figure 4.1) is the basic modification to create a 3D structure, which creates a cone-shaped auxiliary network after n-generation network. The parameter γ in equation (4.34) will be identical to:

$$\gamma_n = \frac{\sum_{i=1}^{n} 2^{(3i-1)/3}}{\sum_{i=1}^{n} 2^{(1-i)/3}}. \tag{4.37}$$

Another approach is using a 3-branches bifurcation, which forms a tetrahedron at a bifurcation node, instead of a 2-branches. Therefore, the n-generation radii will be smaller than 2-branches bifurcation

$$r_n = 3^{(n/3)} r_k, \tag{4.38}$$

and the angle between a branch to the connecting line is a constant for any generation branch

$$\cos\theta_n = \sqrt{2/3}. \tag{4.39}$$

Inserting equation (4.39) into (4.25) yields

$$L_k = 2\sqrt{2/3}(L_1 + L_2 + ... + L_n). \tag{4.40}$$

Since we assume $L_n \propto r_n$, the n-generation vessel length is $L_n = 3^{(\frac{1-n}{3})} L_1$, revers to equation (4.38). Then, equation (4.40) reduces to

$$L_k = 2\sqrt{2/3} L_1 \left(1 + 3^{-\frac{1}{3}} + ... + 3^{\frac{1-n}{3}}\right). \tag{4.41}$$

The electric circuit representation for this 3D structure differs an additional branch for each 2-branches from 2D auxiliary network in figure 4.3.

$$R = \frac{2R_1}{3} + \frac{2R_2}{9} + ... + \frac{2R_n}{3^n}. \tag{4.42}$$

Inserting Poiseuille equation (4.3), (4.5) and (4.38) results

$$R = \frac{8L_k}{\pi r_k^4} \left(\frac{\sum_{i=1}^{n} \mu(3^{-i/3} r_k) 3^{8(i-2)/3}}{\sum_{i=1}^{n} 3^{-i/3}} \sqrt{\frac{2}{3}} \right) \tag{4.43}$$

or parameter γ:

$$\gamma_n = \left(\frac{\sum_{i=1}^{n} 3^{8(i-2)/3}}{\sum_{i=1}^{n} 3^{-i/3}} \sqrt{\frac{2}{3}} \right). \tag{4.44}$$

If we change the angle θ_n in equation (4.39), parameter γ will be altered accordingly.

4.5 The transport equation

Transport processes are the primary functions of blood circulation in the human body, such as the transport of oxygen and metabolic waste, as well as the transport of tracer agents. In general, advective and diffusive processes govern this transport. Given the blood flux field $\mathbf{v}_i$ and the diffusivity $\mathcal{D}_i$ in the domain Ω_i, the conservation of the scalar quantity c_i is given by the conservation equation

$$\frac{\partial (\phi_i c_i)}{\partial t} + \nabla \cdot (c_i \mathbf{v}_i - \mathcal{D}_i \nabla c_i) = q_c \quad \text{in } \Omega_i \tag{4.45}$$

where q_c is the source/sink term. The source term in the Darcy model is blood perfusion from another compartment, as well as inflow and outflow from the vascular terminal. The gadolinium tracer diffusivity by dynamic-contrast-enhanced MRI was estimated to be $2.08(\pm 0.88) \times 10^4 \text{mm}^2/\text{s}$ based on in vivo measurements [33]. Indicator diffusion in a compartment is instantaneous, based on the conservation of indicator mass (3.4) and the well-mixed compartment model described in Chapter 3. As a result, the diffusion term is neglected, and the rate of change of the tracer within the control volume yields

$$\int_{\Omega_i} \frac{\partial (\phi_i c_i)}{\partial t} = -\frac{1}{\Omega_i} \int_{\partial \Omega_i} c_\beta (\mathbf{v}_\beta \cdot \mathbf{n}) dA + q_c. \tag{4.46}$$

This transport equation is assumed to apply to the transport processes in the vascular network and the direct connection model, with a porosity of one, and the source/sink term represents the vascular network's input/output.

Chapter 5

Numerical model

The first topic in this chapter is the discretization of vascular structures, including the vascular network as a macrocirculation and the direct connection model introduced in the previous chapters. Section 5.2 provides an overview of discretization of tissue as a porous medium, while Section 5.4 focuses on temporal discretization. The final section contains details on how to combine the models for the entire vascular system in an organ while accounting for both microcirculation models.

5.1 Vascular network discretization

The imaging data is used to derive the arterial and venous vascular networks. This data segmentation directly provides a discretization of vascular segments and nodes for the entire vascular network. The governing equation in the vascular network is simply a 0D flow model, which can be observed in dedicated medical imaging acquisitions. A system of equations in a fully linearized model is governed by (4.3) and the conservation of flow in the vascular network. In the case of a nonlinear system, the vessel elasticity (4.9) and pressure drop at junctions (4.11) are taken into account for the loss of accuracy in the linear model, which causes nonlinearities in the system.

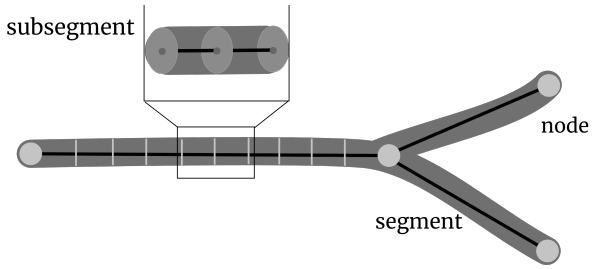

Figure 5.1: The finer vessel discretization description. Each vessel is divided into n subsegments representing voxels in a cylindrical region. This voxel tracer concentration value then gives contrast for mimicking medical image data.

In order to map tracer concentration in a more detailed image, a finer discretization of vascular segment is constructed. According to the required image resolution, each vessel segment i is divided into n_i subsegments associated with central axis voxels, and every remaining voxel in the segment is assigned to the closest central axis point, resulting in disc-like discretization volumes referring to subsegment within a segment [23].

5.2 Darcy discretization

The Darcy equations (4.18) in the capillary bed are solved using a two-point flux approximation (TPFA). First, we compute the fluid transmissibility between adjacent cells i and j,

$$\tau_{ij} = 2S_{ij}\left(\frac{\Delta x_i \mu_i}{\mathbf{K}_{\beta,i}} + \frac{\Delta x_j \mu_j}{\mathbf{K}_{\beta,j}}\right)^{-1} \tag{5.1}$$

where S_{ij} is the face area between cells i and j, and, as above $\beta \in \{a, v\}$. Because of the homogeneity of the system, constant parameters and uniform discretization, equation (5.1) simplifies to

$$\tau_{ij} = S\frac{\mathbf{K}_\beta}{\mu \Delta x}. \tag{5.2}$$

Then, applying TPFA to (4.15) in single cell i and adjacent cells $j \in N_i$, neighbour cells around i, we obtain

$$\sum_{j \in N_i} \tau_{ij}(P_i - P_j) = Q_i. \tag{5.3}$$

Applying this procedure for all cells in the domain, we obtain a system of equations $\mathbf{A_D x} = \mathbf{b}$, where $\mathbf{A}_D$ is a symmetric matrix with elements

$$a_{ik} = \begin{cases} \sum_{j \in N_i} \tau_{ij} & \text{if } k = i \\ -\tau_{ik} & \text{if } k \neq i. \end{cases} \tag{5.4}$$

We note that while the TPFA method is not a consistent discretization for general grids, but it will be consistent and convergent on the quadrilateral grids used in this study [1].

5.3 Model implementation

This section explains how to implement a multiple-scale model. In terms of microcirculation models, there are two options for simulating the entire vascular system in an organ:

- **Hybrid model** that combines a vascular network model (Section 4.2) and a porous media model (Section 4.3) into a (nonlinear) system of equations.

- **Connection model** that uses a direct connection model (Section 4.4) to connect the observable (macrocirculation) arteries to the nearest vein terminal nodes.

In general, the system of equation can be written in matrix form as $\mathbf{Ax} = \mathbf{b}$, where $\mathbf{A}$ is the resistance matrix for vessels in the whole vascular system, $\mathbf{x}$ is the unknown vector consisting of the pressure and the volumetric flow rate in each vessel and $\mathbf{b}$ is the vector of pressures in the inlet and outlet nodes as the boundary conditions. The macrocirculation and the microcirculation models are combined in a (nonlinear) system of equations

$$\begin{pmatrix} \mathbf{A}_{N-N} & \mathbf{A}_{N-T} & 0 \\ \mathbf{A}_{T-N} & \mathbf{A}_{T-T} & \mathbf{A}_{T-M} \\ 0 & \mathbf{A}_{M-T} & \mathbf{A}_{M-M} \end{pmatrix} \begin{pmatrix} \mathbf{x}_N \\ \mathbf{x}_T \\ \mathbf{x}_M \end{pmatrix} = \begin{pmatrix} \mathbf{b}_N \\ 0 \\ 0 \end{pmatrix}. \tag{5.5}$$

The indexes N and T refer to the internal and terminal nodes in the vascular network, and index M stands for the microcirculation discretization. The unknown $\mathbf{x}$ consists of

$$\mathbf{x}_N = \begin{pmatrix} \mathbf{p}_N \\ \mathbf{q}_N \end{pmatrix}$$
$$\mathbf{x}_T = \mathbf{p}_T$$
$$\mathbf{x}_M = \begin{pmatrix} \mathbf{p}_M \\ \mathbf{q}_M \end{pmatrix},$$

where $\mathbf{p}$ and $\mathbf{q}$ are the pressure at the nodes and flow rate in the corresponding segment, respectively. The blocks matrices represent systems of equations in the following domains:

- Matrix $\mathbf{A}_{N-N} \in \mathbf{R}^{N \times N}$ is a matrix representation of the vascular graph model's system of nonlinear equations. It is based on equation (4.12), (4.9), and conservation of mass. It consists of as many equations as the number of vessels and nodes in the internal nodes network. It also has no more than four nonzero entries per row.

- Matrix $\mathbf{A}_{T-T} \in \mathbf{R}^{T \times T}$ is the system of nonlinear equations on terminal nodes at the coupling between the vascular graph and the microcirculation model. It is based on equation (4.12) and (4.9). The matrix is a diagonal matrix.

- Matrices $\mathbf{A}_{N-T} \in \mathbf{R}^{N \times T}$ and $\mathbf{A}_{T-N} \in \mathbf{R}^{T \times N}$ are couplings between the internal nodes and the terminal nodes from equations (4.12), (4.9), and conservation of mass.

- Matrix $\mathbf{A}_{M-M} \in \mathbf{R}^{M \times M}$ is the system of equation for microcirculation. The hybrid model uses the system of linear equations based on the Darcy's law discretization in equation (5.4). It has the same number of variables as the number of discretization cells in the capillary domain and is symmetric. The direct connection vessel (Section

4.4) is used in the connection model, and the flow resistance is represented by a matrix based on equation (4.43).

- Matrices $\mathbf{A}_{M-T} \in \mathbf{R}^{M\times T}$ and $\mathbf{A}_{T-M} \in \mathbf{R}^{T\times M}$ are couplings between the terminal nodes and microcirculation. The pressure and mass continuity are based on equation (4.22) and (4.21) for the hybrid model. The connection model, on the other hand, simply assumes equal pressure and flow rate in the coupling vessel (the conservation of mass and energy).

- The $\mathbf{b}_N$ term in the RHS is from the boundary conditions of the circulation system's inlet and outlet in Section 4.2.4.

We propose the specific solution to equation 5.5. The model will be solved efficiently according to the model type (hybrid and connection model).

Hybrid model The hybrid model consists of linear and nonlinnear system in the governing equations (5.5). The linear Darcy discretization system of equations (matrix $\mathbf{A}_{M-M}$) is solved separately and then combined back into the governing equation using the Schur complement method. The nonlinear system is then solved iteratively. Let

$$\mathbf{B} = \begin{pmatrix} \mathbf{A}_{T-T} & \mathbf{A}_{T-M} \\ \mathbf{A}_{M-T} & \mathbf{A}_{M-M} \end{pmatrix}.$$

The Schur complement of block $\mathbf{A}_{M-M}$ for the matrix $\mathbf{B}$ is defined as $\mathbf{B}/\mathbf{A}_{M-M} := \mathbf{A}_{T-T} - \mathbf{A}_{T-M}\mathbf{A}_{M-M}^{-1}\mathbf{A}_{M-T}$. $\mathbf{A}_{M-M}^{-1}$ is not computed explicitly, due to of the large size of the matrix. Instead, the system of linear equation $\mathbf{A}_{M-M}\mathbf{C} = \mathbf{A}_{M-T}$ is solved giving $\mathbf{C} = \mathbf{A}_{M-M}^{-1}\mathbf{A}_{M-T}$. The linear system can easily be solved using, for instance, a LU factorization. Substituting back in matrix $\mathbf{A}$ (5.5), we have

$$\begin{pmatrix} \mathbf{A}_{N-N} & \mathbf{A}_{N-T} \\ \mathbf{A}_{T-N} & \mathbf{B}/\mathbf{A}_{M-M} \end{pmatrix} \begin{pmatrix} \mathbf{x}_N \\ \mathbf{x}_T \end{pmatrix} = \begin{pmatrix} \mathbf{b}_N \\ 0 \end{pmatrix}. \tag{5.6}$$

The above nonlinear system (5.6) is solved using an iterative nonlinear least square optimization algorithm based on Powell's dogleg method [54]. The solution of the linearized system (by omitting the nonlinearities) is used as the nonlinear solver's initial approximation value. More information about this implementation can be found in Paper A.

The problem is defined as a nonlinear minimization problem, and it is solved using the Levenberg–Marquardt and Powell's dogleg methods in this thesis. Occlusion experiments in paper A are used to evaluate the methods for accuracy and robustness. The results of Powell's dogleg method are more robust than those of the Levenberg–Marquardt method. In varying percentages of occlusion, Powell's method consistently converges.

Connection model In comparison to the hybrid model, the system in equation (5.5) is a nonlinear system of equations with fewer linear equations. The direct connection model produces as many linear equations as there are close connections between the observable veins and arteries. In this case, the Schur complement method is ineffective, so the system is solved directly by a nonlinear solver. To solve the nonlinear system in the hybrid model, we use Powell's dogleg method. In paper B, the network flow model that generates synthetic MRI data uses the direct connection model as the microcirculation.

5.4 Temporal discretization of tracer

Tracer movements in the vascular system are mapped as time-series data based on equation (4.46). A temporal discretization is necessary to solve the equation and find the time-series tracer distribution. Consider the time derivative of concentration C in a discrete cell, given by a function S,

$$\frac{\partial C}{\partial t} = S(C)$$

The function $S(C)$ is obtained from the solution of blood flow model in Section 5.3. The volumetric blood flow determines the rate of concentration change in cell i as follows,

$$S(C) = \sum_{j \in N_{\text{influx}}} \frac{C_j Q_j}{vol_j} - \frac{C_i}{vol_i} \sum_{jin N_{\text{outflux}}} Q_j,$$

where N_{influx} denotes the adjacent upstream cells, vol_i is the volume of cell i, and N_{outflux} is the adjacent downstream cells. The time derivative can be replaced by a finite difference approximation at discrete time points. The unknown concentration at the next time step, C^{k+1}, can be obtained from the solution at the current time step, C^k, by the theta rule:

$$C^{k+1} = C^k + \left[\theta S(C^{k+1}) + (1-\theta) S(C^k)\right] \Delta t \tag{5.7}$$

where Δt is the time step and θ in $[0, 1]$ is a given parameter. We use $\Delta t = 3 \times 10^{-4}$ s for (0 s, 120 s) interval in the simulation. In equation (5.7), $\theta = 1$ defines the implicit Euler scheme, $\theta = 0$ gives the explicit Euler scheme, and $\theta = 0.5$ gives the Crank-Nicolson scheme.

This modeling framework can be implemented in either a 2D or 3D domain. In this thesis, we use the explicit Euler scheme. The other schemes will be computationally expensive to implement, and there will be no benefit to using them in this framework. In the explicit Euler method, we ensure tracer mass conservation by scaling the final tracer mass of the calculation to its initial mass in each iteration. As a result, the tracer mass that increases to and decreases from the domain is maintained to come solely from

arterial and venous input and output. In order to reduce the error, we use a small Δt.

Chapter 6

Summary and outlook

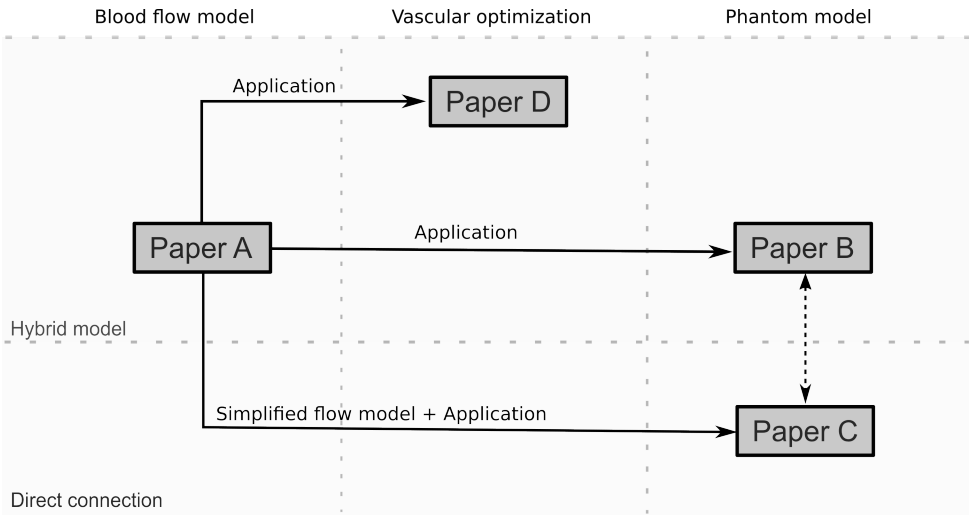

Figure 6.1: An overview of the papers in the thesis and their connections. A solid line denotes an existing connection, whereas a dashed line denotes a potential connection and comparable relation. The papers are split into two categories: flow models and applications.

6.1 Summary of papers

Part I of the thesis concludes with a summary of the papers and their relationships. Figure 6.1 sketches the research topic dealt within each paper and connection between them.

Paper A examines the nonlinearity effects in our multi-scale blood flow model and presents the mathematical basis for the hybrid flow model. Nonlinearities in the model are caused by pressure correction due to vessel elasticity and estimation of pressure drop at vessel junctions. In this paper, we demonstrate our framework using a 2D anatomical frog tongue and validate it using experimental data.

A simplified model from Paper A is used in Paper B to synthesize tracer concentration flow data from DCE-MRI. Instead of the dual-compartment Darcy flow model described in paper A, a single-compartment Darcy flow model is used for the capillary bed. The simulation produces a qualitatively accurate tracer concentration flow as well as a good starting point for future development in the clinical application. However, assuming a constant and uniform permeability in the Darcy model has a disadvantage because the microcirculation flow is observed as a circle spread of tracer around the terminal nodes.

In paper C, we create a network flow model framework that serves as a reference for tracer-kinetic models. The direct connection simplifies the microcirculation in paper A and B by replacing the Darcy model. The framework proposed here is used to compare four traditional pharmacokinetics models of varying complexity. The experiments show that the modeling framework can help with the development of digital phantom models in a variety of ways.

Paper D is a vascular network optimization application based on paper A. In macrocirculation, the vascular network's structure, such as length and angle, is optimized. We hypothesized that the vascular network is optimally designed to feed the tissue within an organ so that the tissue will receive nutrients equally regardless of its location from the arterial root of the organ. We compare and evaluate the optimization objective in this study using blood fluxes and time of flight within the microcirculation. The results show that time-of-flight optimization is more robust than flux optimization. The study, however, is limited to simple geometry, which creates an unrealistic vasculature in nature.

An extended summary of each paper is presented below. As the first author of the papers, I have contributed by designing, writing the necessary software, implementing, analyzing and discussing the results, and writing the manuscript. The other authors have also participated in the study's design and methodological selection, as well as discussion of the findings and feedback on the writing.

Paper A: A nonlinear multi-scale model for blood circulation in a realistic vascular system

Ulin Nuha A. Qohar, Antonella Zanna Munthe-Kaas, Jan Martin Nordbotten and Erik Andreas Hanson (2021), published in the Royal Society Open Science Journal.
DOI: https://doi.org/10.1098/rsos.201949

The effects of nonlinearity in our developed multiscale blood flow model are investigated in this paper. The framework is made up of a coupling of vascular network flow describing macrocirculation and a hybrid flow model for microcirculation in an organ's entire

vascular system. The vascular model is based on Poiseuille's law, with pressure correction by elasticity and pressure drop estimation at vessels junctions. Darcy's law is used to model the porous capillary bed as a two-compartment domain (artery and venous). The fluid exchange between the arterial and venous capillary bed compartments is referred to as blood perfusion. We show our framework on a 2D anatomical frog tongue from a textbook and validate it with experimental data. The numerical experiments demonstrate that the proposed blood circulation model is 1) highly dependent on the structure and parameters of both the vascular vessels and the capillary bed, and 2) provides a realistic blood circulation in the organ. The proposed model has the advantage of being complex enough to reliably capture the main underlying physiological function while also being extremely adaptable in terms of incorporating various local effects. Furthermore, the model's numerical implementation is straightforward, allowing simulations to be run on a standard desktop computer.

Paper B: A multi-scale flow model for studying blood circulation in vascular system

Ulin Nuha A. Qohar, Antonella Zanna Munthe-Kaas, Jan Martin Nordbotten and Erik Andreas Hanson (2020), Proceeding of the European Conference on Numerical Mathematics and Advanced Applications (ENUMATH 2019).
DOI: http://dx.doi.org/10.1007/978-3-030-55874-1_73

Paper B shows how to replicate perfusion imaging data using the framework developed in Paper A for tracer concentration flow simulation. This work is the preliminary work for creating a digital reference object capable of producing synthetic perfusion MRI data. Numerical experiments show that blood circulation is closely related to the vascular system's structure and functional parameters. The simulations generate tracer concentration flows that are qualitatively realistic. A constant parameter for permeability in Darcy, on the other hand, demonstrates an unrealistic flow within microcirculation, where the tracer flow is not exchanged locally within the capillary bed connected to the nearest artery and vein. This model served as the foundation for further development in paper C, which included a modification for microcirculation.

Paper C: Network flow simulation as digital reference in DCE-MRI tracer kinetic model validation

Ulin Nuha Abdul Qohar, Steven Sourbron, Antonella Zanna Munthe-Kaas, Erik Andreas Hanson (2022), submitted to Magnetic Resonance in Medicine Journal.

In paper C, we create a network flow model framework in a realistic vascular system that serves as a reference for tracer-kinetic models. The proposed model is based on a macrocirculation vascular graph model and a direct connection model that connects the observable arteries and veins (microcirculation). It is assumed that the injected contrast agent (CA) particles will flow passively along with the bloodstream. We compare four traditional pharmacokinetics models of varying complexity to demonstrate the potential application of the proposed framework. The experiments indicate that the modelling framework may provide several contributions to the development of digital phantom models. First, the synthetic data demonstrates the possibility of a more detailed evaluation of the elusive problem of model bias than was previously possible. Second, it may bring new light to the understanding of AIF placement. While localized AIFs eliminate the problem of bolus dispersion, they increase parameter estimation errors in the compartment models. Third, the proposed network flow model is well-suited for a traditional one-compartment-based model (1CM and MS).

Paper D: **A Study of Vascular Structure Optimization Using Hybrid Flow Model**

Ulin Nuha A. Qohar, Antonella Zanna Munthe-Kaas, Jan Martin Nordbotten and Erik Andreas Hanson (2021), Preprint

The vascular structure in nature is believed to be an optimized design for delivering nutrients to tissues and carrying metabolic waste back to the heart. In this paper, we attempt to find a mathematical optimization that describes the construction of a vascular network. The model is based on the multi-scale framework described in paper A, with the structure of the vascular network as the macrocirculation optimized. The optimization objective is based on the fluxes and time-of-flight in microcirculation, which is the capillary bed tissue in the model. The flux optimization yields several local minima, and the TOF is consistent with the outcome. This study, however, was unable to accurately represent the vascular structure found in nature. The outcome provides some insight into the method for determining the mathematical structure underlying this problem.

6.2 Outlook

We have shown that the system of human blood circulation is a complex system to simulate in full scale. By using a multi-scale framework, can be simplified while still able to capture complex behaviours. Paper A describes a nonlinear multi-scale framework

that induces nonlinearities due to the Fåhræus-Lindqvist effect, vessel elasticity, and pressure drop at the junction. Other nonlinearities, including but not limited to blood vessel curvature, plasma skimming, and precapillary sphincters, can be easily added to the framework by modifying it. The model can also be numerically treated in the same manner, using the Schur complement approach and solving for all nonlinearities in the same Newton iteration. The model formulation allows also for a study of the effect of each nonlinearity, and can provide a better understanding of the complexity of blood circulation.

Paper B presents a tracer generator based on the multi-scale flow model from paper A. The results show that a lack of correct modeling parameters can result in understanding unphysical behaviour like the tracer to take a very long time in some specific microcirculation regions, as well as a circular spread of the tracer from the arterial terminals. This study could be extended to include a physiological parameter derived from perfusion imaging data, such as the permeability distribution of tissue derived from DCE-MRI data, which would result in a more accurate tracer simulation. Darcy microcirculation could limit blood flow from an arterial node to the nearest vein nodes by creating a heterogeneous permeability. Finding the physiologically relevant permeability is thus another option for future studies. When the permeability is changed from orthogonal to heterogeneous, the two-point flux approximation (TPFA) may encounter a problem. There are TPFA modifications that attempt to solve this problem by either locating the degree of freedom at the circumcenter or introducing nonlinear transmissibility. Another option for overcoming this limitation is to use conforming polyhedron meshes.

The difficulty in defining permeability without using perfusion imaging data inspired the study in paper C. The study's goal is to generate synthetic data to be used for validating perfusion tracer kinetic models. As a result, the model must be built independently of the tracer kinetic models that calculate perfusion parameters. This research can be expanded into a vascular network by using an imaging modality such as MRA (Magnetic Resonance Angiography), which produces a well-defined segmented vascular network. Future research will also necessitate more accurate simulation of key imaging characteristics such as limited spatial resolution and partial volume effects.

The study in paper D continues by extending the model into a 3D structure based on real image data of an organ, i.e. extracting arterial network using ToF-MRA image, identifying vein vasculature using QSM, and segmenting tissues and organ boundary using T1-weighted anatomical 3D data. Within the brain numerical domain, the alteration can be limited to a certain extent. Another option is to grow the vascular network from the existing vascular network in order to recover the unobservable vascular network, which can then be validated using perfusion imaging data.

As a final note, the work of this thesis embraces the principle of open science, by sharing computational codes and data along with the papers. There are already numerous open-sources and codes available in the context of blood flow modeling, and this work is only a minor contribution by the author to the development of digital reference objects. The primary reason for sharing the code is to support the reproducibility of scientific results, which accelerates scientific progress in this field.

Bibliography

[1] Aavatsmark, I. (2007), Interpretation of a two-point flux stencil for skew parallelogram grids, *Computational Geosciences*, *11*(3), 199–206, doi:10.1007/s10596-007-9042-1. 5.2

[2] Betts, M. J., J. Acosta-Cabronero, A. Cardenas-Blanco, P. J. Nestor, and E. Düzel (2016), High-resolution characterisation of the aging brain using simultaneous quantitative susceptibility mapping (qsm) and r2* measurements at 7 t, *Neuroimage*, *138*, 43–63. 1

[3] Boyer, L., I. Leguerney, S. R. Thomas, V. Grand-Perret, N. Lassau, and S. Pitre-Champagnat (2018), Study of the reliability of quantification methods of dynamic contrast-enhanced ultrasonography: numerical modeling of blood flow in tumor microvascularization, *Physics in Medicine & Biology*, *63*(17), 17NT01. 1.1

[4] Burggren, W. W., J. E. Bicudo, M. L. Glass, and A. S. Abe (1992), Development of blood pressure and cardiac reflexes in the frog pseudis paradoxsus, *American Journal of Physiology-Regulatory, Integrative and Comparative Physiology*, *263*(3), R602–R608, doi:10.1152/ajpregu.1992.263.3.R602, pMID: 1415648. 1.1

[5] Calamante, F. (2013), Arterial input function in perfusion MRI: A comprehensive review, *Progress in Nuclear Magnetic Resonance Spectroscopy*, *74*, 1 – 32, doi:https://doi.org/10.1016/j.pnmrs.2013.04.002. 3.4

[6] Calamante, F., D. G. Gadian, and A. Connelly (2000), Delay and dispersion effects in dynamic susceptibility contrast mri: simulations using singular value decomposition, *Magnetic Resonance in Medicine: An Official Journal of the International Society for Magnetic Resonance in Medicine*, *44*(3), 466–473. 3.4

[7] Calamante, F., D. G. Gadian, and A. Connelly (2003), Quantification of bolus-tracking mri: improved characterization of the tissue residue function using tikhonov regularization, *Magnetic Resonance in Medicine: An Official Journal of the International Society for Magnetic Resonance in Medicine*, *50*(6), 1237–1247. 3.4

[8] Chnafa, C., K. Valen-Sendstad, O. Brina, V. Pereira, and D. Steinman (2017), Improved reduced-order modelling of cerebrovascular flow distribution by accounting for arterial bifurcation pressure drops, *Journal of Biomechanics*, *51*, 83 – 88, doi: https://doi.org/10.1016/j.jbiomech.2016.12.004. 1, 4.2.4

[9] Cohnheim, J. F. (1872), *Untersuchungen über die embolischen Prozesse*, Berlin: Hirschwald. 4.1

[10] Darcy, H. (1856), Les fontaines publique de la ville de dijon, p. 570. 4.3.2

[11] Donahue, K. M., R. M. Weisskoff, and D. Burstein (1997), Water diffusion and exchange as they influence contrast enhancement, *Journal of Magnetic Resonance Imaging*, *7*(1), 102–110. 1

[12] Donaldson, S. B., C. M. West, S. E. Davidson, B. M. Carrington, G. Hutchison, A. P. Jones, S. P. Sourbron, and D. L. Buckley (2010), A comparison of tracer kinetic models for t1-weighted dynamic contrast-enhanced mri: Application in carcinoma of the cervix, *Magnetic Resonance in Medicine*, *63*(3), 691–700. 3.3.3, 3.3.4

[13] Duan, C., J. F. Kallehauge, G. L. Bretthorst, K. Tanderup, J. J. Ackerman, and J. R. Garbow (2017), Are complex DCE-MRI models supported by clinical data?, *Magnetic resonance in medicine*, *77*(3), 1329–1339. 1

[14] El-Bouri, W. K., and S. J. Payne (2015), Multi-scale homogenization of blood flow in 3-dimensional human cerebral microvascular networks, *Journal of Theoretical Biology*, *380*, 40 – 47, doi:https://doi.org/10.1016/j.jtbi.2015.05.011. 1, 2.1.1, 4.4

[15] El-Bouri, W. K., and S. J. Payne (2018), Investigating the effects of a penetrating vessel occlusion with a multi-scale microvasculature model of the human cerebral cortex, *NeuroImage*, *172*, 94 – 106, doi:https://doi.org/10.1016/j.neuroimage.2018.01.049. 2.1

[16] Formaggia, L., F. Nobile, A. Quarteroni, and A. Veneziani (1999), Multiscale modelling of the circulatory system: a preliminary analysis, *Computing and visualization in science*, *2*(2-3), 75–83. 4.2.3, 4.3

[17] Gaa, T., W. Neumann, S. Sudarski, U. I. Attenberger, S. O. Schönberg, L. R. Schad, and F. G. Zöllner (2017), Comparison of perfusion models for quantitative T1 weighted DCE-MRI of rectal cancer, *Scientific Reports*, *7*(1), 1–9. 1

[18] Gould, I. G., P. Tsai, D. Kleinfeld, and A. Linninger (2017), The capillary bed offers the largest hemodynamic resistance to the cortical blood supply, *Journal of Cerebral Blood Flow & Metabolism*, *37*(1), 52–68. 1.1

[19] Hanson, E. A., and A. Lundervold (2013), Local/non-local regularized image segmentation using graph-cuts, *International Journal of Computer Assisted Radiology and Surgery*, *8*(6), 1073–1084, doi:10.1007/s11548-013-0903-x. 4.1

[20] Hanson, E. A., C. Sandmann, A. Malyshev, A. Lundervold, J. Modersitzki, and E. Hodneland (2018), Estimating the discretization dependent accuracy of perfusion in coupled capillary flow measurements, *PloS one*, *13*(7), e0200,521. 3.3

[21] Harteveld, A. A., L. J. De Cocker, N. Dieleman, A. G. van der Kolk, J. J. Zwanenburg, P. A. Robe, P. R. Luijten, and J. Hendrikse (2015), High-resolution post-contrast time-of-flight mr angiography of intracranial perforators at 7.0 tesla, *PLoS One*, *10*(3), e0121,051. 1

[22] Heye, A. K., M. J. Thrippleton, P. A. Armitage, M. d. C. V. Hernández, S. D. Makin, A. Glatz, E. Sakka, and J. M. Wardlaw (2016), Tracer kinetic modelling for DCE-MRI quantification of subtle blood–brain barrier permeability, *Neuroimage*, *125*, 446–455. 1

[23] Hodneland, E., E. Hanson, O. Sævareid, G. Nævdal, A. Lundervold, V. Šoltészová, A. Z. Munthe-Kaas, A. Deistung, J. R. Reichenbach, and J. M. Nordbotten (2019), A new framework for assessing subject-specific whole brain circulation and perfusion using MRI-based measurements and a multi-scale continuous flow model, *PLOS Computational Biology*, *15*(6), 1–31, doi:10.1371/journal.pcbi.1007073. 1, 1.1, 2.1, 4.1, 4.3.2, 4.3.3, 5.1

[24] Hodneland, E., X. Hu, and J. M. Nordbotten (2020), Well-posedness, discretization and preconditioners for a class of models for mixed-dimensional problems with high dimensional gap, *arXiv preprint arXiv:2006.12273*. 4.3.3

[25] Hooper, G. (1977), Diameters of bronchi at asymmetrical divisions, *Respiration Physiology*, *31*(3), 291 – 294, doi:https://doi.org/10.1016/0034-5687(77)90072-X. 2.2

[26] Horsfield, K., and M. J. Woldenberg (1989), Diameters and cross-sectional areas of branches in the human pulmonary arterial tree, *The Anatomical Record*, *223*(3), 245–251, doi:10.1002/ar.1092230302. 2.2

[27] Huang, W., R. T. Yen, M. McLaurine, and G. Bledsoe (1996), Morphometry of the human pulmonary vasculature, *Journal of Applied Physiology*, *81*(5), 2123–2133. 2.2

[28] Ingrisch, M., and S. Sourbron (2013), Tracer-kinetic modeling of dynamic contrast-enhanced MRI and CT: a primer, *Journal of pharmacokinetics and pharmacodynamics*, *40*(3), 281–300. 3.3

[29] Kallehauge, J. F., K. Tanderup, C. Duan, S. Haack, E. M. Pedersen, J. C. Lindegaard, L. U. Fokdal, S. M. I. Mohamed, and T. Nielsen (2014), Tracer kinetic model selection for dynamic contrast-enhanced magnetic resonance imaging of locally advanced cervical cancer, *Acta Oncologica*, *53*(8), 1064–1072. 1

[30] Kamiya, A., and T. Togawa (1972), Optimal branching structure of the vascular tree, *The bulletin of mathematical biophysics*, *34*(4), 431–438, doi:10.1007/BF02476705. 2.2

[31] Kassab, G. S., and Y.-C. B. Fung (1995), The pattern of coronary arteriolar bifurcations and the uniform shear hypothesis, *Annals of Biomedical Engineering*, *23*(1), 13–20, doi:10.1007/BF02368296. 2.2

[32] Khalifa, F., A. Soliman, A. El-Baz, M. Abou El-Ghar, T. El-Diasty, G. Gimel'farb, R. Ouseph, and A. C. Dwyer (2014), Models and methods for analyzing DCE-MRI: A review, *Medical physics*, *41*(12), 124,301. 1, 3.3

[33] Koh, T., S. Hartono, C. Thng, T. Lim, L. Martarello, and Q. Ng (2013), In vivo measurement of gadolinium diffusivity by dynamic contrast-enhanced mri: A preclinical study of human xenografts, *Magnetic resonance in medicine*, *69*(1), 269–276. 4.5

[34] Koh, T. S., S. Bisdas, D. M. Koh, and C. H. Thng (2011), Fundamentals of tracer kinetics for dynamic contrast-enhanced MRI, *Journal of Magnetic Resonance Imaging*, *34*(6), 1262–1276. 3.2, 3.3, 3.3.3

[35] Landis, E. M. (1931), Capillary pressure and hyperemia in muscle and skin of the frog, *American Journal of Physiology-Legacy Content*, *98*(4), 704–716. 1.1

[36] Larsson, C., M. Kleppestø, I. Rasmussen Jr, R. Salo, J. Vardal, P. Brandal, and A. Bjørnerud (2013), Sampling requirements in DCE-MRI based analysis of high grade gliomas: simulations and clinical results, *Journal of Magnetic Resonance Imaging*, *37*(4), 818–829. 1

[37] Mirramezani, M., and S. C. Shadden (2020), A distributed lumped parameter model of blood flow, *Annals of Biomedical Engineering*, *48*(12), 2870–2886. 1

[38] Murray, C. D. (1926), The physiological principle of minimum work applied to the angle of branching of arteries, *Journal of General Physiology*, *9*(6), 835–841. 2.2

[39] Murray, C. D. (1926), The physiological principle of minimum work. i. the vascular system and the cost of blood volume, *Proceedings of the National Academy of Sciences of the United States of America*, *12*(3), 207–214. 2.2, 4.4.2

[40] Mynard, J. P., and K. Valen-Sendstad (2015), A unified method for estimating pressure losses at vascular junctions, *International Journal for Numerical Methods in Biomedical Engineering*, *31*(7), n/a–n/a, doi:10.1002/cnm.2717, cnm.2717. 1, 4.2.4, 4.2.4

[41] Nejad-Davarani, S. P., H. Bagher-Ebadian, J. R. Ewing, D. C. Noll, T. Mikkelsen, M. Chopp, and Q. Jiang (2017), An extended vascular model for less biased estimation of permeability parameters in DCE-T1 images, *NMR in Biomedicine*, *30*(6), e3698. 1.1

[42] Nordsletten, D. A., S. Blackett, M. D. Bentley, E. L. Ritman, and N. P. Smith (2006), Structural morphology of renal vasculature, *American Journal of Physiology - Heart and Circulatory Physiology*, *291*(1), H296–H309, doi:10.1152/ajpheart.00814.2005. 2.2

[43] Olufsen, M. S., C. S. Peskin, W. Y. Kim, E. M. Pedersen, A. Nadim, and J. Larsen (2000), Numerical simulation and experimental validation of blood flow in arteries with structured-tree outflow conditions, *Annals of Biomedical Engineering*, *28*(11), 1281–1299, doi:10.1114/1.1326031. 1, 4.4.2

[44] Olufsen, M. S., A. Nadim, and L. A. Lipsitz (2002), Dynamics of cerebral blood flow regulation explained using a lumped parameter model, *American Journal of Physiology-Regulatory, Integrative and Comparative Physiology*, *282*(2), R611–R622, doi:10.1152/ajpregu.00285.2001, pMID: 11792673. 4.2.1, 4.4.2

[45] Pant, S., B. Fabrèges, J.-F. Gerbeau, and I. E. Vignon-Clementel (2014), A methodological paradigm for patient-specific multi-scale cfd simulations: from clinical measurements to parameter estimates for individual analysis, *International Journal for Numerical Methods in Biomedical Engineering*, *30*(12), 1614–1648, doi:10.1002/cnm.2692. 4.2.1

[46] Passerini, T., M. d. Luca, L. Formaggia, A. Quarteroni, and A. Veneziani (2009), A 3D/1D geometrical multiscale model of cerebral vasculature, *Journal of Engineering Mathematics*, *64*(4), 319, doi:10.1007/s10665-009-9281-3. 1

[47] Payne, S. J. (2017), *Cerebral Blood Flow and Metabolism: A Quantitative Approach*, World Scientific. 4.2.4

[48] Peladeau-Pigeon, M., and C. Coolens (2013), Computational fluid dynamics modelling of perfusion measurements in dynamic contrast-enhanced computed tomography: development, validation and clinical applications, *Physics in Medicine & Biology*, *58*(17), 6111. 1.1

[49] Perdikaris, P., L. Grinberg, and G. E. Karniadakis (2016), Multiscale modeling and simulation of brain blood flow, *Physics of Fluids*, *28*(2), 021,304, doi:10.1063/1.4941315. 1

[50] Perl, W., N. Lassen, and R. Effros (1975), Matrix proof of flow, volume and mean transit time theorems for regional and compartmental systems, *Bulletin of mathematical biology*, *37*, 573–588. 3.1, 3.1.1

[51] Peyrounette, M., Y. Davit, M. Quintard, and S. Lorthois (2018), Multiscale modelling of blood flow in cerebral microcirculation: Details at capillary scale control accuracy at the level of the cortex, *PLOS ONE*, *13*(1), 1–35, doi:10.1371/journal.pone.0189474. 1, 2.1, 2.1.1, 4.1, 4.3, 4.4

[52] Pishko, G. L., G. W. Astary, T. H. Mareci, and M. Sarntinoranont (2011), Sensitivity analysis of an image-based solid tumor computational model with heterogeneous vasculature and porosity, *Annals of biomedical engineering*, *39*(9), 2360. 1.1

[53] Possenti, L., S. di Gregorio, F. M. Gerosa, G. Raimondi, G. Casagrande, M. L. Costantino, and P. Zunino (2019), A computational model for microcirculation including fahraeus-lindqvist effect, plasma skimming and fluid exchange with the tissue interstitium, *International Journal for Numerical Methods in Biomedical Engineering*, *35*(3), e3165, doi:10.1002/cnm.3165, e3165 cnm.3165. 2.4

[54] Powell, M. J. (1968), A fortran subroutine for solving systems of nonlinear algebraic equations, *Tech. rep.*, Atomic Energy Research Establishment, Harwell, England (United Kingdom). 5.3

[55] Quarteroni, A., A. Veneziani, and C. Vergara (2016), Geometric multiscale modeling of the cardiovascular system, between theory and practice, *Computer Methods in Applied Mechanics and Engineering*, doi:10.1016/j.cma.2016.01.007. 1, 2.1, 4.2.1, 4.3

[56] Qureshi, M. U., G. D. A. Vaughan, C. Sainsbury, M. Johnson, C. S. Peskin, M. S. Olufsen, and N. A. Hill (2014), Numerical simulation of blood flow and pressure drop in the pulmonary arterial and venous circulation, *Biomechanics and Modeling in Mechanobiology*, *13*(5), 1137–1154, doi:10.1007/s10237-014-0563-y. 1, 4.4

[57] Reichold, J., M. Stampanoni, A. L. Keller, A. Buck, P. Jenny, and B. Weber (2009), Vascular graph model to simulate the cerebral blood flow in realistic vascular networks, *Journal of Cerebral Blood Flow & Metabolism*, *29*(8), 1429–1443, doi:10.1038/jcbfm.2009.58, pMID: 19436317. 1, 1.1, 4.1, 4.2.1, 4.4

[58] Rohan, E., V. Lukeš, and A. Jonášová (2018), Modeling of the contrast-enhanced perfusion test in liver based on the multi-compartment flow in porous media, *Journal of mathematical biology*, *77*(2), 421–454. 1

[59] Rossitti, S., and J. Löfgren (1993), Vascular dimensions of the cerebral arteries follow the principle of minimum work., *Stroke*, *24*(3), 371–377, doi:10.1161/01.STR.24.3.371. 2.2

[60] Secomb, T. W., and A. R. Pries (2013), Blood viscosity in microvessels: experiment and theory, *Comptes Rendus Physique*, *14*(6), 470–478. 2.4, 4.2.2

[61] Shipley, R. J., A. F. Smith, P. W. Sweeney, A. R. Pries, and T. W. Secomb (2019), A hybrid discrete–continuum approach for modelling microcirculatory blood flow, *Mathematical Medicine and Biology: A Journal of the IMA*, *37*(1), 40–57, doi:10.1093/imammb/dqz006. 1, 2.1, 4.2.1

[62] Singh, A., R. K. S. Rathore, M. Haris, S. K. Verma, N. Husain, and R. K. Gupta (2009), Improved bolus arrival time and arterial input function estimation for tracer kinetic analysis in DCE-MRI, *Journal of Magnetic Resonance Imaging: An Official Journal of the International Society for Magnetic Resonance in Medicine*, *29*(1), 166–176. 1

[63] Sourbron, S. (2014), A tracer-kinetic field theory for medical imaging, *IEEE transactions on medical imaging*, *33*(4), 935–946. 1

[64] Sourbron, S., and D. L. Buckley (2011), Tracer kinetic modelling in MRI: estimating perfusion and capillary permeability, *Physics in Medicine & Biology*, *57*(2), R1. 3.1

[65] Sourbron, S., M. Ingrisch, A. Siefert, M. Reiser, and K. Herrmann (2009), Quantification of cerebral blood flow, cerebral blood volume, and blood–brain-barrier leakage with dce-mri, *Magnetic Resonance in Medicine: An Official Journal of the International Society for Magnetic Resonance in Medicine*, *62*(1), 205–217. 3.3.3, 3.3.4

[66] Sourbron, S. P., and D. L. Buckley (2013), Classic models for dynamic contrast-enhanced MRI, *NMR in Biomedicine*, *26*(8), 1004–1027. 1, 3, 3.1, 3.2, 3.3

[67] Stucht, D., K. A. Danishad, P. Schulze, F. Godenschweger, M. Zaitsev, and O. Speck (2015), Highest resolution in vivo human brain mri using prospective motion correction, *PloS one*, *10*(7), e0133,921. 1, 2.1.1

[68] Takahashi, T. (2014), *Branching Systems of Fractal Vascular Trees*, pp. 1–24, Springer Japan, Tokyo, doi:10.1007/978-4-431-54508-8_1. 2.2

[69] Takahashi, T., T. Nagaoka, H. Yanagida, T. Saitoh, A. Kamiya, T. Hein, L. Kuo, and A. Yoshida (2009), A mathematical model for the distribution of hemodynamic parameters in the human retinal microvascular network, *Journal of Biorheology*, *23*(2), 77–86, doi:10.1007/s12573-009-0012-1. 2.2

[70] Uylings, H. (1977), Optimization of diameters and bifurcation angles in lung and vascular tree structures, *Bulletin of Mathematical Biology*, *39*(5), 509 – 520, doi:https://doi.org/10.1016/S0092-8240(77)80054-2. 2.2

[71] van de Vosse, F. N., and N. Stergiopulos (2011), Pulse wave propagation in the arterial tree, *Annual Review of Fluid Mechanics*, *43*(1), 467–499, doi:10.1146/annurev-fluid-122109-160730. 4.2.3

[72] Wahyulaksana, G., S. Saporito, J. A. den Boer, I. H. Herold, and M. Mischi (2018), In vitro pharmacokinetic phantom for two-compartment modeling in DCE-MRI, *Physics in Medicine & Biology*, *63*(20), 205,012. 1

[73] Wolfe, R. R., and D. L. Chinkes (2004), *Isotope tracers in metabolic research: principles and practice of kinetic analysis*, John Wiley & Sons. 3.1

[74] Zamir, M. (1976), The role of shear forces in arterial branching., *The Journal of General Physiology*, *67*(2), 213–222, doi:10.1085/jgp.67.2.213. 2.2

[75] Zamir, M. (1999), On fractal properties of arterial trees, *Journal of Theoretical Biology*, *197*(4), 517 – 526, doi:https://doi.org/10.1006/jtbi.1998.0892. 2.2

[76] Zamir, M., and J. A. Medeiros (1982), Arterial branching in man and monkey., *The Journal of General Physiology*, *79*(3), 353–360, doi:10.1085/jgp.79.3.353. 2.2

Part II

Included Papers

Paper A

A nonlinear multi-scale model for blood circulation in a realistic vascular system

Ulin Nuha A. Qohar, Antonella Zanna Munthe-Kaas, Jan Martin Nordbotten and Erik Andreas Hanson (2021)
Royal Society Open Science Journal,

ROYAL SOCIETY OPEN SCIENCE

royalsocietypublishing.org/journal/rsos

Research

Cite this article: Qohar UNA, Zanna Munthe-Kaas A, Nordbotten JM, Hanson EA. 2021 A nonlinear multi-scale model for blood circulation in a realistic vascular system. *R. Soc. Open Sci.* **8**: 201949.
https://doi.org/10.1098/rsos.201949

Received: 31 October 2020
Accepted: 28 October 2021

Subject Category:
Mathematics

Subject Areas:
applied mathematics/biomechanics/bioengineering

Keywords:
blood flow, Darcy, multi-scale model, perfusion, porous media, vascular system

Author for correspondence:
Ulin Nuha A. Qohar
e-mail: ulin.qohar@uib.no

A nonlinear multi-scale model for blood circulation in a realistic vascular system

Ulin Nuha A. Qohar, Antonella Zanna Munthe-Kaas, Jan Martin Nordbotten and Erik Andreas Hanson

Department of Mathematics, University of Bergen, Allegaten 41, Bergen 5008, Norway

UNAQ, 0000-0003-3747-4878

In the last decade, numerical models have become an increasingly important tool in biological and medical science. Numerical simulations contribute to a deeper understanding of physiology and are a powerful tool for better diagnostics and treatment. In this paper, a nonlinear multi-scale model framework is developed for blood flow distribution in the full vascular system of an organ. We couple a quasi one-dimensional vascular graph model to represent blood flow in larger vessels and a porous media model to describe flow in smaller vessels and capillary bed. The vascular model is based on Poiseuille's Law, with pressure correction by elasticity and pressure drop estimation at vessels' junctions. The porous capillary bed is modelled as a two-compartment domain (artery and venous) using Darcy's Law. The fluid exchange between the artery and venous capillary bed compartments is defined as blood perfusion. The numerical experiments show that the proposed model for blood circulation: (i) is closely dependent on the structure and parameters of both the larger vessels and of the capillary bed, and (ii) provides a realistic blood circulation in the organ. The advantage of the proposed model is that it is complex enough to reliably capture the main underlying physiological function, yet highly flexible as it offers the possibility of incorporating various local effects. Furthermore, the numerical implementation of the model is straightforward and allows for simulations on a regular desktop computer.

1. Introduction

Nowadays, computational approaches have become one of the complementary tools in studying structure, function and blood regulation of the vascular systems [1–10]. The fundamental purpose of developing a numerical model is to understand how changes in the vascular structure affect transport mechanisms in organs, giving important clinical information. However, one of

THE ROYAL SOCIETY PUBLISHING

the challenging modelling issues for these systems is the fact that vascular systems are made of vessels at different scales [8], ranging from large arteries with close to turbulent blood flow, to smaller arteries and arterioles with mostly laminar flow, and to capillaries, with perfusion of cellular particles between artery and vein capillaries. This complexity makes it difficult to fully understand the connection between scales and the effect of localized changes on the whole organ.

The multi-scale mathematical modelling for blood circulation offers a reasonable solution to these difficulties. By combining the well-established flow models at various vascular scale levels, one may achieve a global model that also takes into account multiple local properties. The coupling between each level is the key to creating a complete model with a suitable balance between computational cost and detail, as required for pathological characterization [6,8,11]. To this end, several earlier studies have proposed suitable modelling set-ups [1,5,7,12–16]. The authors in [5] propose a three-dimensional/one-dimensional coupling for combining large and small arteries in the cerebral vasculature. In [10], the authors consider a network representation that includes arteries, veins and capillaries. This model assumes that the whole vasculature is an interconnected tube network and results in a much larger system. However, the computational cost of this approach limits its applicability at a clinically relevant scale. To overcome the limitation, the authors in [10] replaced the capillaries and arterioles with a coarser network with similar resistivity. In a recent study [3], the authors treat vessels as a one-dimensional network model and the capillary bed as a three-dimensional continuum model, thus decreasing significantly the computational cost and allowing for full brain simulations. Other works addressing a discrete-continuum system have investigated the blood flow simulation for cerebral and liver microvasculature, both in humans and animals [7,12,17,18]. It must be mentioned, however, that zero-dimensional and one-dimensional models have a reduction in accuracy when compared to full three-dimensional models, in particular when applied to describe large vessels [19].

In the current work, we propose a multi-scale model for blood circulation that incorporates nonlinearities induced by the vascular structure. The blood flow in the vascular network (arteries and veins) is described using a vascular graph model [10] in which vessel segments are represented as long cylindrical tubes with constant radii. To compensate for the accuracy loss of this model, a model for pressure drop is included at vessel bifurcations [19,20] and we allow for a vessel radius dependence on pressure due to vessel elasticity [21]. Darcy flow is used to describe the continuum representation of the micro-circulation in the smaller vessels and the capillary bed. Further, a continuous distribution is introduced to model the unresolved structure between the vascular network terminals and the Darcy domain, with the purpose of reflecting the micro-vessel structure surrounding each terminal node. Differently from [3], we investigate the impact of nonlinear interactions between pressure and flow, as well as the role of vessel bifurcations in the flow network, and the effect of vessel occlusion in an organ. Our model was developed for full-organ simulations with parameters from experiment data on frogs [22–25] accompanied by estimations [21,26–28] to obtain results purely from governing equations and the given anatomy.

2. Material and methods

In this section, we present our modelling framework. We construct a system consisting of an arterial and venous vascular network, a two-compartment capillary bed and the couplings between the parts. A realization of the model configuration is illustrated in figure 1, where the dotted line represents the coupling and connection between compartments. Blood flows from the roots of the arterial network (bottom left) through the arterial network (red), then to the continuous domains of the capillary compartments (light red for arterial and light blue for venous compartment), and finally to the venous network structure (blue) and to the venous roots at the bottom right of the venous network. The arterial and venous terminal nodes are connected to the respective continuous capillary domains in the capillary bed (red solid and blue dashed dotted-lines).

2.1. Model simplifications and hypotheses

Our modelling framework is quite generic and, as such, does not take into account all micro and macro effects related to the flow in the vascular system. Yet, by expressing the system in a multi-scale framework, we manage to capture some of the underlying micro-scale details using the macro-scale parameters.

The main simplification in this model is that the capillary bed is assumed to be a homogeneous and isotropic porous media. Further, the nonlinearities induced by the capillary physiology and the blood

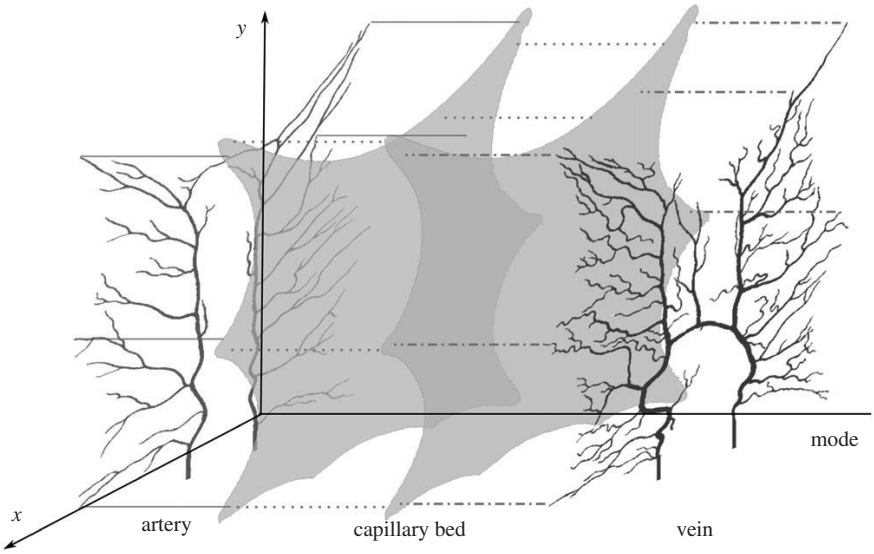

Figure 1. The quasi-three-dimensional numerical model for a two-dimensional spatial problem. The *xy* (vertical) axis represents the two-dimensional computational domain in space and the third axis (horizontal) is the model axis. Blood flows from the roots of the arterial network through the arterial network (red), then to the continuous domains of the capillary compartments (light red for arterial and light blue for venous compartment) and finally to the venous network structure (blue) and to the venous roots at the bottom of the venous network. The arterial and venous terminal nodes are connected to their respective continuous capillary domains in the capillary bed (red solid and blue dashed dotted lines). The green dotted lines represent the pixel-wise bridge between capillary compartments, which is modelled as the blood perfusion in §2.4.

itself are neglected [29]. These include, among others, the non-Newtonian behaviour of the blood [30], the Fahraeus–Lindqvist effect [31], plasma skimming [32] as well as viscoelasticity in the capillary bed. The effect of these limitations is partly studied in a recent simulation framework [33]. Nevertheless, the reported simulations are only performed on a micro-scale and, to our knowledge, no current simulation framework is able to incorporate all these micro-effects into a multiscale model.

With the simplifications mentioned above, the nonlinearities in this work are restricted to effects arising from and affecting the vascular network, namely pressure drop at bifurcations and vessel elasticity. Other than that, we limit our model to situations where the structure of the vascular system is in a fixed passive condition (steady-state), so that all parameters and coefficients are constant over the simulation time.

2.2. Graph structure model for vascular networks

A system of equations was constructed based on a network structure for both arteries and veins. Assuming laminar flow and non-slip conditions on the vessel walls, each vessel segment n was modelled as a long cylindrical tube of length L_n with constant radius $r_n \ll L_n$. The vessel radius was computed as an average radius value from the segmentation data. The pressure drop ΔP_n in a single vessel segment n was computed using Hagen–Poiseuille's Law [10]

$$\Delta P_n^h = \frac{8\mu L_n q_n}{\pi r_n^4}, \tag{2.1}$$

where the upper index h stands for hydrodynamic, μ is the blood viscosity and q_n is a volumetric blood flow. At a junction node, a pressure match scheme was used to define vessel pressure drop connected to the junction node [34]. An additional pressure drop estimation was defined from [19,20]

$$\Delta P_n^b = \frac{\rho q_{\text{dat}}^2}{2\pi^2 r_{\text{dat}}^4}\left(1 + \frac{q_n^2 r_{\text{dat}}^4}{q_{\text{dat}}^2 r_n^4} - \frac{2 q_n r_{\text{dat}}^2}{q_{\text{dat}} r_n^2}\cos\left(\frac{3}{4}\theta_{(\text{dat},n)}\right)\right), \tag{2.2}$$

where the upper index b stands for bifurcation and the index dat refers to the datum vessel, i.e. the vessel from which the flow approaches the junction. Further, $\theta_{(\text{dat},n)}$ is the angle between the datum vessel and

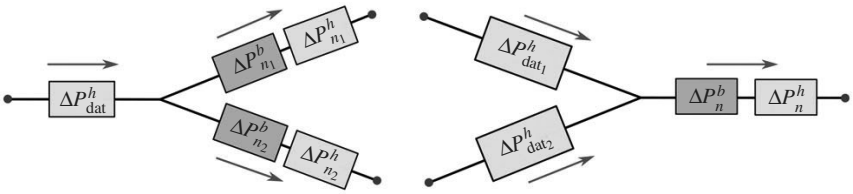

Figure 2. Illustration of pressure drop at junctions, see (2.3). The arrow represents the direction of blood flow.

vessel n. The pressure drop equation was constructed based on Bernoulli equation to match the total pressure at the inlet and outlet vessels at bifurcation. The derivation details were described in [20] for converging and diverging flow at a junction. Hence, the total pressure drop after a bifurcation node was computed as the sum of both equations (2.1) and (2.2)

$$\Delta P_n = \Delta P_n^h + \Delta P_n^b, \tag{2.3}$$

see figure 2. The other governing equation was the conservation of mass at a node

$$\sum q_{\text{in}} = \sum q_{\text{out}}, \tag{2.4}$$

with q_{in} representing the blood that flows into the node and q_{out} is a flow out of the node.

2.3. Elasticity on vessel walls

Vessel wall elasticity provides capacitance and pulse-wave dampening, allowing the arteries to maintain a relatively constant pressure despite the pulsating nature of the blood flow. On the other hand, the vessel wall elasticity also allows for a vessel radius dependence on the pressure gradient, to regulate blood supply in case of an alteration of the vascular system [21]. The change in radius due to pressure was described by

$$\Delta r = r - r_{\text{init}} = \frac{(1-\lambda^2) r_{\text{init}}^2}{hE} (P_{\text{in}} - P_{\text{ext}}), \tag{2.5}$$

where r_{init} is the initial vessel radius without pressure gradient, h is the vessel wall thickness, E is the Young modulus, λ is the Poisson ratio, and P_{in}, P_{ext} are the pressures inside and outside the vessel, respectively. The vessel thickness is assumed to be proportional to the vessel radius, with $h = 0.22r$ for the arteries and $h = 0.1r$ for the veins. This is within the approximated range reported in [24]. For the elasticity parameters, the Young modulus in the arteries E_a is two times bigger than E_v in the veins, $E_a = 2E_v = 1$ MPa, and $\lambda = 0.5$ [21,27]. P_{in} is defined as the average pressure in the segment, that is the average pressures at both segment endpoints, and P_{ext} as the capillary pressure at the midpoint outside the vessel. The elasticity equation (2.5) has the effect of introducing a nonlinearity to the system. Thus, the pressure difference between two adjacent nodes in a vessel is determined by substituting equation (2.5) into equations (2.1) and (2.2).

2.4. Capillary model

In the capillary model, smaller vessels and the capillary bed were discretized with a uniform grid and described by Darcy's single-phase flow equation. Darcy's Law, describing the flow of a fluid in a porous medium, states that a fluid flows from regions of higher pressure to regions of lower pressure in a linear manner. Thus

$$\mathbf{v} = -\frac{\mathbf{K}}{\mu} \nabla P, \tag{2.6}$$

where $\mathbf{v}$ is the Darcy flux (volumetric flow rate per unit area ($\text{m}^3\ \text{s}^{-1}\ \text{m}^{-2}$)), $\mathbf{K}$ is the permeability tensor of the porous medium and μ is the viscosity [35]. In addition, we assume conservation of mass (continuity equation)

$$\nabla \cdot \mathbf{v} = Q, \tag{2.7}$$

where Q is the source term (s^{-1}). In this model, Q is a source or sink, for instance describing the flow in or out a terminal node in the arterial or venous system, or describing the passage of flow from one compartment to the other. We assume blood to be an incompressible fluid, and by incorporating Darcy flow into the continuity

equation, we obtain

$$-\nabla \cdot \left(\frac{\mathbf{K}}{\mu}\nabla P\right) = Q. \tag{2.8}$$

The capillary bed is described as a two-compartment system, using one compartment for the arterial part and one for the venous part. Blood perfusion is interpreted as the interchange between the two compartments, i.e. the exchange of oxygenated blood with deoxygenated blood in the capillary bed. The driving force for perfusion is the pressure difference between the two compartments [3], giving the linear relation

$$F = \alpha(P_a - P_v), \tag{2.9}$$

where α is the perfusion parameter. The Darcy model for the two compartments becomes

$$\left.\begin{aligned} -\nabla \cdot \left(\tfrac{\mathbf{K}_a}{\mu}\nabla P_a\right) &= Q_a - \alpha(P_a - P_v) \quad \text{in } \Omega_a \\ -\nabla \cdot \left(\tfrac{\mathbf{K}_v}{\mu}\nabla P_v\right) &= Q_v + \alpha(P_a - P_v) \quad \text{in } \Omega_v \\ \text{and} \qquad u_\beta \cdot n_\beta &= 0 \quad \text{(Neumann BC)} \qquad \text{on } \partial\Omega_\beta, \end{aligned}\right\} \tag{2.10}$$

where Ω_β is the Darcy capillary volume and the index $\beta = \{a, v\}$ stands for artery and vein, respectively.

2.5. Coupling vascular structure and capillary models

To complete the system, both the arterial and venous Darcy systems were combined with the terminal nodes of the arterial and venous networks as point sources/sinks. The analytic solution of the Darcy equation around these points is a Dirac delta function, with a singularity at the source/sink point, creating a problem at the three-dimensional–one-dimensional interface. To avoid this problem, a fluid distribution function was introduced [3]

$$f(x) = \begin{cases} C\exp\left(\frac{-1}{1-|x|^2}\right) & \text{if } |x| < 1 \\ 0 & \text{if } |x| \geq 1, \end{cases} \tag{2.11}$$

and this function was used with a finite radius ε, $f^\varepsilon(x) = f(x/\varepsilon)$ on the Darcy domain. The finite radius ε can be set to a user-chosen constant or to a fraction of the terminal vessel's radius. In this manuscript, it is set to three pixels to represent the vessels that are not observable in the imaging data. As a result, the flow at a terminal node Q_t is coupled to the capillary compartment as a number of sources/sinks $Q_\beta(x)$ according to the relation

$$Q_t^\epsilon = \int_{\Omega_\beta} Q_\beta(x) f^\epsilon(x - x_t)\mathrm{d}x. \tag{2.12}$$

Beside mass continuity, we have to describe pressure continuity between the one-dimensional vascular graph and the three-dimensional Darcy model. The pressure drop between the terminal node t and the surrounding tissue was thus given as

$$P_t - \int_{\Omega_\beta} P_\beta(x) f^\epsilon(x - x_l)\mathrm{d}x = \kappa Q_t, \tag{2.13}$$

where κ represents the resistance estimation for capillary system around terminal t in the Darcy model. In this work, the resistance κ was estimated as a constant by using equation (2.1) to compute the resistance of a cylindrical tube connecting a terminal node to the Darcy domain inside the sphere of radius ε centred at the terminal node. The tube has a length of ε and a radius of $m^{-1/3}r_t$, where m is the number of computational cells within the sphere.

Both flow and pressure couplings between the vascular graph and Darcy model close the loop from the arterial roots to the venous roots. While a well-posedness analysis of the full model with nonlinear effects is beyond the scope of this paper, a linearized model similar to the one considered in this paper was recently shown to be well posed, both in the continuous setting and when discretized by low-order finite volume methods [36].

2.6. Numerical implementation of the flow

2.6.1. The vascular network

It consists of vessel segments and nodes and is governed by (2.1), (2.4) and (2.11). For each graph segment n, the pressure drop (2.1) (linear part) and the pressure drop at junctions (2.2) (nonlinear part) were considered. When considering elasticity, equation (2.5) was used.

The equations at the nodes are of three different types: at the root nodes, we have control equations/boundary conditions (given with the problem); at the internal nodes (connecting two or more segments) we have conservation of volume (2.4), and at the terminal nodes we have coupling equations with the Darcy model. In our four roots terminal (two arterial and two venous roots), there were several options to assign the boundary conditions.

Five further control equations must be considered for the system to have a unique solution. These were constructed by assigning constant pressure on the arterial and the venous root nodes (Dirichlet BC) and conservation of mass for the whole system

$$P_{\text{root},\beta} = P_{\text{BC}} \tag{2.14}$$

and

$$\sum_{n \in N_{\text{root}}} q_n = 0, \tag{2.15}$$

where root, $\beta = a$, v is a root node on the arterial or the venous structure, P_{BC} represents the constant pressure on two arterial roots (input) and two venous roots (output), and N_{root} are root segments, with $q_n > 0$ for the artery and $q_n < 0$ for the vein. Finally, the whole complex is represented as a system of nonlinear equations $\mathbf{F}(\mathbf{x}) = \mathbf{b}$, where $\mathbf{F}(\mathbf{x}) = \mathbf{A}(\mathbf{x})\mathbf{x}$.

2.6.2. The Darcy domains (capillary bed)

The Darcy equations (2.10) in the capillary bed were solved using a two-point flux approximation (TPFA) on a uniform grid. We assume that the permeability $\mathbf{K}$ in the capillary bed is constant and uniform, and represent it by K (scalar). First, we computed the fluid transmissibility between adjacent cells i and j,

$$\tau_{ij} = 2S_{ij}\left(\frac{\Delta x_i \mu_i}{K_{\beta,i}} + \frac{\Delta x_j \mu_j}{K_{\beta,j}}\right)^{-1}, \tag{2.16}$$

where S_{ij} is the face area between cells i and j, and, as above $\beta \in \{a, v\}$. Because of the homogeneity of the system, constant parameters and uniform discretization, equation (2.16) simplifies to

$$\tau_{ij} = S\frac{K_\beta}{\mu \Delta x}. \tag{2.17}$$

Then, applying TPFA to (2.6) in single cell i and adjacent cells $j \in N_i$, neighbour cells around i, we obtain

$$\sum_{j \in N_i} \tau_{ij}(P_i - P_j) = Q_i. \tag{2.18}$$

Applying this procedure for all cells in the domain, we obtain a system of equations $\mathbf{A}_{D-D}\mathbf{x} = \boldsymbol{b}$, where $\mathbf{A}_{D-D}$ is a symmetric matrix with elements

$$a_{ik} = \begin{cases} \sum_{j \in N_i} \tau_{ij} & \text{if } k = i \\ -\tau_{ik} & \text{if } k \neq i. \end{cases} \tag{2.19}$$

We note that while the TPFA method is not a consistent discretization for general grids, it is consistent and convergent on the uniform grids used in this study [37].

2.6.3. The full coupling

Finally, the vascular networks and the Darcy domains were combined in a (nonlinear) system of equations $\mathbf{A}\mathbf{x} = \mathbf{b}$, $\mathbf{A} = \mathbf{A}(\mathbf{x})$, with unknown $\mathbf{x}$ consisting of the pressure and the flow rate in the model

$$\begin{pmatrix} \mathbf{A}_{N-N} & \mathbf{A}_{N-T} & 0 \\ \mathbf{A}_{T-N} & \mathbf{A}_{T-T} & \mathbf{A}_{T-D} \\ 0 & \mathbf{A}_{D-T} & \mathbf{A}_{D-D} \end{pmatrix} \begin{pmatrix} \mathbf{x}_N \\ \mathbf{x}_T \\ \mathbf{x}_D \end{pmatrix} = \begin{pmatrix} \mathbf{b}_N \\ 0 \\ 0 \end{pmatrix}. \tag{2.20}$$

The indexes N and T refer to the internal and terminal nodes in the vascular network, and index D stands for the Darcy equation discretization. The unknown $\mathbf{x}_N$ is the pressure at the internal nodes and flow rate in the corresponding segment, $\mathbf{x}_T$ is the pressure in the terminal nodes, and $\mathbf{x}_D$ is the pressure on the Darcy domain. The blocks matrices represent systems of equations in the following domains:

- Matrix $\mathbf{A}_{N-N} \in \mathbf{R}^{N\times N}$ is a matrix representation of the vascular graph model's system of nonlinear equations. It is based on equations (2.3)–(2.5) and consists of as many equations as the number of vessels and nodes in the internal nodes network. It also has no more than four non-zero entries per row.
- Matrix $\mathbf{A}_{T-T} \in \mathbf{R}^{T\times T}$ is the system of nonlinear equations on terminal nodes at the coupling between the vascular graph and the capillary model. It is based on equations (2.3) and (2.5). The matrix is a diagonal matrix.
- Matrices $\mathbf{A}_{N-T} \in \mathbf{R}^{N\times T}$ and $\mathbf{A}_{T-N} \in \mathbf{R}^{T\times N}$ are couplings between the internal nodes and the terminal nodes from equations (2.3)–(2.5).
- Matrix $\mathbf{A}_{D-D} \in \mathbf{R}^{D\times D}$ is the system of linear equations based on the Darcy's Law discretization in equation (2.19). Its number of variables is the number of discretization cells in the capillary domain and the system is symmetric.
- Matrices $\mathbf{A}_{D-T} \in \mathbf{R}^{D\times T}$ and $\mathbf{A}_{T-D} \in \mathbf{R}^{T\times D}$ are couplings between the terminal nodes and Darcy discretization cells. The pressure and mass continuity are based on equations (2.13) and (2.12).
- The $\mathbf{b}_N$ term in the r.h.s. is from the boundary conditions of the circulation system in equation (2.14).

Despite the nonlinearity in the governing equations, it can be solved efficiently by using the Schur complement method. Let

$$\mathbf{B} = \begin{pmatrix} \mathbf{A}_{T-T} & \mathbf{A}_{T-D} \\ \mathbf{A}_{D-T} & \mathbf{A}_{D-D} \end{pmatrix}.$$

The Schur complement of block $\mathbf{A}_{D-D}$ for the matrix $\mathbf{B}$ is defined as $\mathbf{B}/\mathbf{A}_{D-D} := \mathbf{A}_{T-T} - \mathbf{A}_{T-D}\mathbf{A}_{D-D}^{-1}\mathbf{A}_{D-T}$. $\mathbf{A}_{D-D}^{-1}$ is not computed explicitly, due to of the large size of the matrix. Instead, the system of linear equation $\mathbf{A}_{D-D}\mathbf{C} = \mathbf{A}_{D-T}$ is solved giving $\mathbf{C} = \mathbf{A}_{D-D}^{-1}\mathbf{A}_{D-T}$. Substituting back in matrix $\mathbf{A}$ (2.20), we have

$$\begin{pmatrix} \mathbf{A}_{N-N} & \mathbf{A}_{N-T} \\ \mathbf{A}_{T-N} & \frac{\mathbf{B}}{\mathbf{A}_{D-D}} \end{pmatrix} \begin{pmatrix} \mathbf{x}_N \\ \mathbf{x}_T \end{pmatrix} = \begin{pmatrix} \mathbf{b}_N \\ 0 \end{pmatrix}. \tag{2.21}$$

The above nonlinear system (2.21) is solved using an iterative nonlinear least-square optimization algorithm based on the Powell dogleg method [38]. The solution of the linearized system (by omitting the nonlinearities) was used as the initial approximation. The entire framework was solved using MATLAB 2019b on a desktop PC with an Intel(R) Core(TM) i7-7700 CPU 3.60GHz and 32 GB RAM, and the codes and instructions for reproducing the results are included in the dataset [39].

2.7. Vascular structures in image data

The model described above is generic and applicable to any two-dimensional or three-dimensional domain. As an illustrative example, we used the model to simulate blood flow in a frog tongue from a two-dimensional anatomical image from a classical biology textbook [23]. This example resembles a realistic vascular system while still being more easy to visualize, interpret and analyse compared to a full three-dimensional system. A drawback of this choice is that the original sample is not available, thus we cannot validate the correctness of the vessel structure. Furthermore, there is an apparent deformation of the geometry. The vascular networks are simplified into two flat networks, as shown in figure 1 as we do not have information about thickness and curvature in the third dimension. Incorrect vessel structure and incorrect geometry may have an impact on the blood flow in the entire domain, especially for intertwined vessels, which are not captured from the two-dimensional image. Still, we believe that the balance between arteries and veins in the image is highly realistic. Since the application to this two-dimensional domain is included as an illustrative example, a deeper analysis of the limitations is outside the scope of the current work.

Figure 3 shows the original image of the frog tongue, with the physiologist's segmentation of the main vessels. The frog tongue was stretched flat and nailed to a canvas. Thereafter, the trained physiologist manually traced the arterial and venous network structures on it. One may notice that only a few vessels serve the middle part of the tongue.

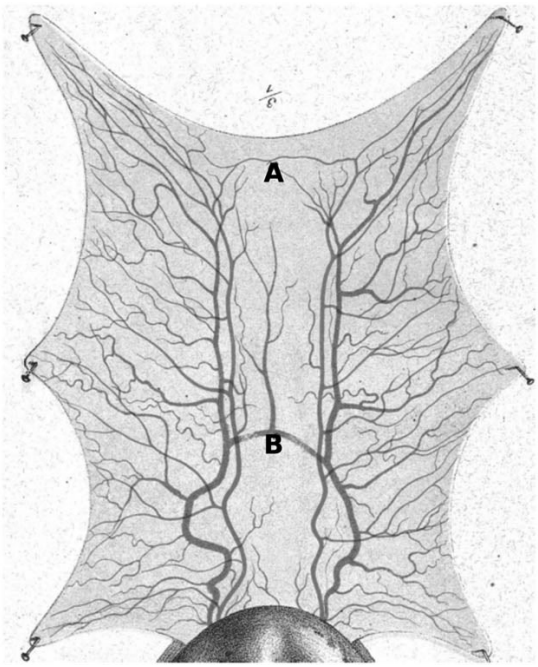

Figure 3. An anatomical frog tongue image from a classical textbook [23], with arterial (red) and venous (blue) vascular network structures. The networks are obtained by segmenting the anatomical vessel structures. Our capillary domain is the region inside the tongue's boundary. Vessel A connects two arterial networks, while Vessel B connects two vein networks.

Table 1. Vascular model parameters.

parameter	value	unit	reference
capillary model size (two-dimensional)	515×634	pixel	—
real size	30.9×38	mm	[23]
porosity of the capillary bed (ϕ)	0.1	dimensionless	[12]
permeability of arterial compartment (K_a)	3×10^{-6}	mm^2	[41]
permeability of venous compartment (K_v)	6×10^{-6}	mm^2	[41]
perfusion parameter (α)	5×10^{-4}	kg^{-1} mm s^{-1}	[3]
viscosity of blood (μ)	$3 \cdot 10^{-6}$	kPa s^{-1}	[3]
artery inlet pressure	30	mmHg	[22]
vein outlet pressure	7.5	mmHg	[24]
Young modulus (E)	1	MPa	[28]
Poisson's ratio (λ)	0.5	dimensionless	[28]
arterial vessel wall thickness ratio	0.22	dimensionless	[24]
venous vessel wall thickness ratio	0.1	dimensionless	[24]

Both the arterial and venous network structures consist of two main vessels (left and right). Our network structure was based on an image segmentation of these using the method in [40]. The small arteries and veins that are near the roots but not visibly connected to the main vessels were discarded in our segmentation, as we need control over inlets and outlets.

We observed that both the arterial and venous networks have some level of anastomoses. The two arterial networks are connected in the uppermost part of the tongue (point A in figure 3) by a small vessel, and the venous networks are connected in the middle of the tongue by a large vessel (point

B). These connected structures have a regulation effect, maintaining blood circulation for the whole organ when some vessel is severed or occluded.

The frog tongue model parameters for our simulations are found in table 1. The real size of the image was estimated based on information from the original source [23]. The pressure inlet is defined as the blood pressure in an average adult frog *Pseudis paradoxsus* [22], and the pressure outlet is assumed to be equal to the average vein pressure in a male frog *Rana pipiens* mesentery [24]. The vessel elasticity parameters were chosen based on the mechanical properties of vessels around those sizes [21,27,28]. The isotropic and homogeneous permeability of the capillary bed was estimated using a simplified Darcy in scalar setting

$$\frac{Q}{A} = -\frac{K_\beta}{\mu}\frac{\Delta P}{\Delta L}, \quad \beta = a, v, \tag{2.22}$$

with frog cerebral cortex values as reference data [42]. The blood velocity is approximately 0.5 mm s^{-1} in an arteriole with length of 2 mm for a pressure drop of $\Delta P = 7.5$ mmHg. We obtain an estimated permeability of 1.2×10^{-6} mm^2. However, the value was adjusted in the simulation (refer to table 1) to match a normal blood flow in veins vessels based on the experimental data in *Rana pipiens*, which is 166.61 ± 21.33 μm s^{-1} (mean ± standard deviation) in the veins with a radius around 10–20 μm [42]. The venous capillary compartment was assumed to be twice as permeable as the arterial capillary compartment.

3. Results and discussion

Using the model proposed above, we have simulated blood flow in several numerical experiments: a baseline model simulation, partial models and linearized simulations, and simulations with vessel occlusions. In particular, the occlusion experiments demonstrate possible applications to the study of blood circulation for an alteration or pathology of the vascular system.

3.1. Baseline model

The baseline model is the fully nonlinear model with nonlinearities due to both pressure drop at junctions as well as vessel elasticity. It was based on equations (2.1), (2.2), (2.4), (2.10), (2.5), (2.12) and (2.13). Figure 4 shows the computed pressure distribution in the whole vascular domain. The simulated pressure distribution has a good resemblance to the experimental data on *Rana pipiens* mesentery in [24]. We see a stronger agreement with the data for the big vessels compared to the smaller vessels close to the capillary bed (labels *a* and *b* in figure 4). The smaller vessels appear to have an overestimated pressure exceeding the observed data slope. This may be caused by rounding discretization effects as the vessel radius approaches pixel size. Further, the frog tongue vascular image from the textbook [23] was hand-drawn with a pen, with no emphasis on estimating diameters. In addition, the tongue was flat-streched, thus deformed from its original shape. The inaccuracy of vessel radii caused by a combination of the three above-mentioned reasons may result in a lower pressure drop across the vessel compared to the anatomically realistic pressure drop (label a in figure 4). We might expect the flow pattern in the system to be impacted accordingly.

The total computational time for the baseline simulation is 82.6 s, with the nonlinear equation (2.21) taking 63.1 s to solve. The total pressure drop in the whole system was 22.5 mmHg (table 1), with the arterial network being the major contributor (71.6% of total). Further, the arterial compartment contributed with 2.7%, the venous compartment with 2.8%, and the vein vascular network had a 5.15 mmHg pressure drop (22.9%). These values are in a realistic range and indicate the importance of the arterial vascular structure to provide the blood circulation through the whole organ. If there is an alteration on an arterial vessel, its impact for the blood circulation will be greater than for a similar vein alteration. The pressure distribution is consistent with the distribution on humans or other animals [25,43,44]. From figure 4, we see that the arterioles are the biggest contributor to the pressure drop in the whole vasculature. The arterioles with a radius less than 100 μm provided 80% of the total pressure drop in the arterial network. In contrast to our result, the numerical experiments in [45] show that the smallest capillary vessels ($r < 5$ μm) contribute the most resistance in the mouse cortex micro-circulation simulation. Their haemodynamic modelling was conducted in a micro-scale vascular network with diameter less

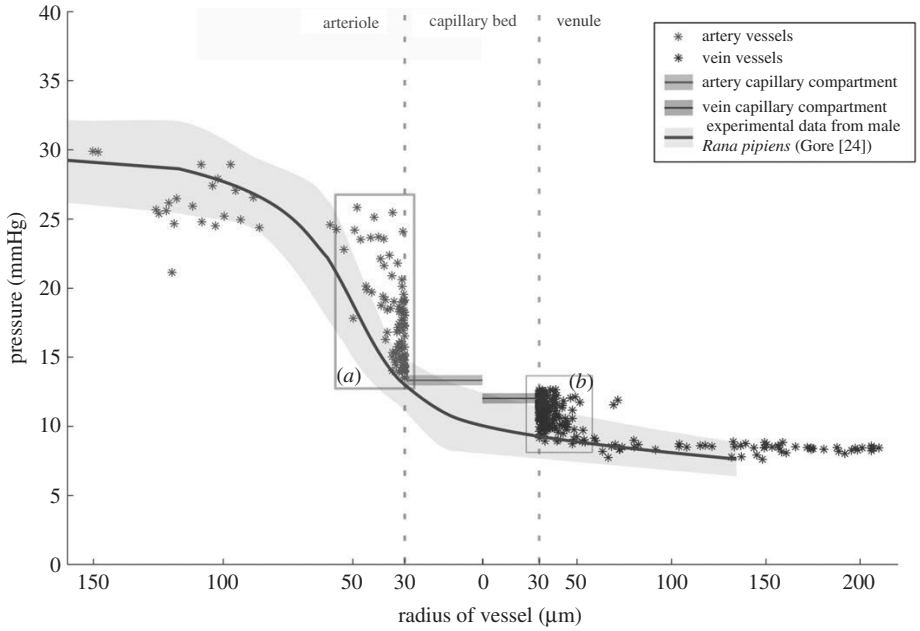

Figure 4. The static blood pressure distribution from our simulations has good estimation across the whole vascular system. The computed pressures (asterisks) follow the effective pressure from experimental data (brown solid line), the light brown area representing the variation from several experimental data measurements [24]. Our simulations produce some overestimation in the small arteriole (label *a*) and venule (label *b*) regions. The inaccurate simulation pressure is likely caused by vessel diameters in the range of the pixel size, so that the rounding of the vessel radius in the segmentation is in mismatch to the true value.

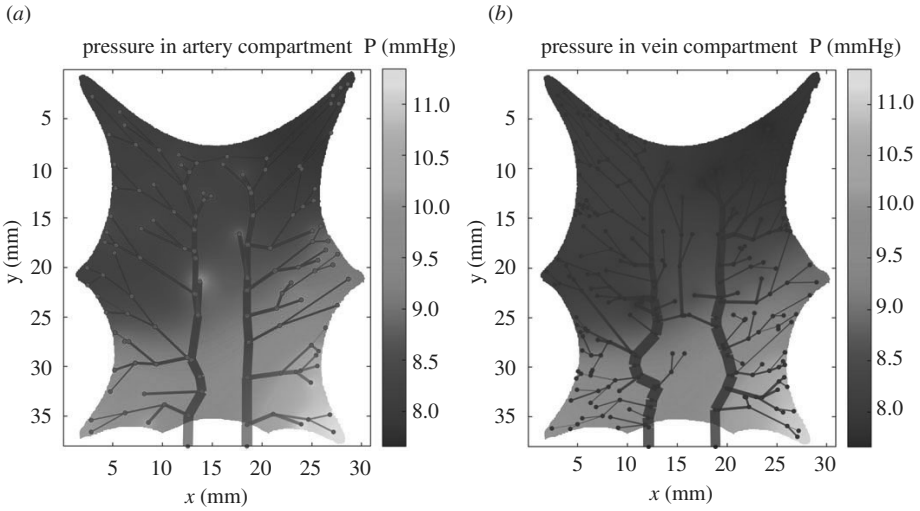

Figure 5. The pressure distribution for the baseline model: the segment thickness in the vascular graphs is proportional to the flow rate passing through it and the local pressure distribution in the Darcy domain. (*a*) The arterial network structure and the arterial compartment with pressure ranging from 7.6 to 11 mmHg (8.6 ± 0.7 mmHg). The right arterial vessel input provides 16% more blood flow compared to the left vessel, causing higher pressure in the right area. (*b*) The vein network structure and venous compartment with pressure ranging from 7.4 to 10.8 mmHg (8.5 ± 0.8 mmHg). The right vein vessel output has 4.3 times more blood flow than the left vessel, playing a vital role in blood distribution in the vein compartment.

than 50 μm, which, in our simulation set-up, is inside the range of the capillary bed (modelled as a Darcy domain). Hence, this particular detail could not be captured in our experiment due to the difference in the simulation scale and set-up.

Table 2. Numerical simulation results for several experiments: flow resistance, like the electrical resistance, is equal to the total pressure drop divided by the total volumetric flow in the system, $R = (P_{in} - P_{out})/Q$ (kg mm^{-4} s^{-1}). The indexes a_N and v_N refer to the arterial and venous vascular networks, the indexes a_C and v_C to the arterial and vein capillary compartments respectively. The total computational time for simulation is denoted by t_{tot}, while t_{sys} refers to the time for the solution of the system (2.21).

simulation	Q_{total} (mm^3 s^{-1})	R_{total} (kg mm^{-4} s^{-1})	R_{a_N}	R_{v_N}	R_{a_C}	R_{v_C}	$t_{tot}(t_{sys})$ (s)
baseline model[a]	1.644	1.825	1.306	0.418	0.049	0.051	82.6 (63.1)
elasticity model[b]	1.646	1.823	1.307	0.416	0.049	0.051	66.5 (47.1)
junction model[c]	1.643	1.825	1.307	0.418	0.049	0.051	90.2 (70.7)
linear model	1.754	1.710	1.319	0.357	0.018	0.017	19.4 (10^{-5})
artery-1 occlusion[a]	1.410	2.127	1.614	0.420	0.046	0.047	3216.4
artery-2 occlusion[a]	1.286	2.332	1.819	0.411	0.050	0.052	374.1
vein-1 occlusion[a]	1.644	1.824	1.297	0.442	0.042	0.044	757.2
vein-2 occlusion[a]	1.554	1.930	1.320	0.488	0.060	0.062	157.1
artery-1 occlusion	1.460	2.054	1.663	0.354	0.019	0.017	20.3
artery-2 occlusion	1.339	2.240	1.850	0.359	0.016	0.015	20.1
vein-1 occlusion	1.724	1.740	1.319	0.387	0.018	0.017	20.1
vein-2 occlusion	1.709	1.755	1.319	0.401	0.018	0.017	20.1

[a]*Baseline model* refers to the fully nonlinear model.
[b]*Elasticity model*: baseline model omitting the pressure drop at junctions equation (2.2).
[c]*Junction model*: baseline model omitting the elasticity equation (2.5). Occlusion: a 50% reduction of the original artery/vein radius.

In [17], the authors demonstrated a qualitatively comparable result to the experimental data using isotropic and homogeneous porous media as the capillary bed in the human cerebral cortex. Our result shows a similar agreement, that is, the dual Darcy compartment provided a good approximation as a replacement for small arterioles, venules and capillaries (see the capillary pressure drop in figure 4). The defined capillary bed covered not only capillaries but also unresolved vessels with diameter less than 60 µm, in which small arterioles and venules are covered. Figure 5 shows the local pressure distribution in the capillary bed. It was observed that the pressure is high around the top edges and low in the left bottom edges of the domain. This result is related to the vascular structure having a small number of branches from the arterial input vessel in the lower region. Pressures at the right area for both compartments are high compared to the left region, reflecting the blood distribution in the vascular network. The right arterial vessel input provides 16% more blood flow compared to the left vessel and the right vein vessel output has 4.3 times more blood flow compared to the left vessel.

Note that there is a good correlation between the pressures in the arterial and venous compartments, see figure 5, as the pressure follows the same distribution in both compartments. The pixel-wise pressure difference between the compartments is expected to be the driving force for local perfusion.

3.2. The partial models and the linearized model

The simulation with the linearized model follows the same set-up as the baseline model, but without the nonlinearities due to vessel elasticity and pressure drops at junctions. We have also tested a setup involving only one of the mentioned nonlinearities at the time (partial models). The macroscopic changes caused by each nonlinearity were compared across the entire system, including the total volumetric flow, total flow resistance and average resistance of the model components. Flow resistance, like an electrical resistance, is equal to the pressure drop divided by the volumetric flow in the system, $R = (P_{in} - P_{out})/Q$ (kg mm^{-4} s^{-1}). The flow resistance of the model component is an approximation; for example, the pressure drop in the arterial network is the difference between the average pressure at the arterial network terminals and the input pressure. In this section, the models are defined as:

— The *Elasticity model*: baseline model omitting the pressure drop at junctions equation (2.2).
— The *Junction model*: baseline model omitting the elasticity equation (2.5).

— The *Linear model*: fully linear model omitting both equations (2.2) (pressure drop at junctions) and (2.5) (elasticity equation) from the baseline model. The linearized model coincides with the model considered in [3]. The solution of this model is used as the initial value for the nonlinear solver in the other models.

3.2.1. Elasticity model

The vessel's elasticity operates similarly to the capacitance in an electrical system. Thus, elasticity can maintain pressure constant by increasing or decreasing the vessel radii. However, this effect also gives additional resistance to blood flow, equivalent to impedance in electricity. Table 2 reports and compares the flow resistance in the system, which is equal to the total pressure drop divided by the total volumetric flow and is analogous to an electrical resistor.

The arterial vessel tends to expand if the pressure in the surrounding Darcy domain is lower than vessel inner pressure. On the other hand, the vein vessel tends to tighten and increase resistance. In our experiments, the elasticity model gives a total resistance of 1.823 kg mm^{-4} s^{-1} (table 2), which is smaller than the baseline model. The elasticity model provided some small differences in arterial flow input and the resistance distribution compared to the baseline model. The computational time is less than the baseline, with the nonlinear system being solved in 47.1 s (table 2). The elasticity model has a shorter running time because it only modifies the Poiseuille equation (2.1) by removing the junction term from the baseline model. The linear model solution is used as the initial value for the nonlinear solver.

3.2.2. Junction model

The pressure drop at the junctions increased the total resistance in the vascular structure, both in arteries and veins [20]. It is also causing the total blood flow in the whole system to decrease, since the volumetric blood flow, Q, changes according to the relation $\Delta P = RQ$. This bifurcation set-up is known as pressure matching at a junction node, which introduces nonlinearity in the flow model [34]. The resistance distribution in the whole system is 0.00069 kg mm^{-4} s^{-1} bigger than the baseline model resistance (after rounding the values, the difference is lost in table 2). The junction model takes slightly longer time than the baseline model, mostly due to taking a longer time to achieve convergence in the nonlinear system.

The junction and the elasticity models only incorporate one of the nonlinear equations into the system at a time. Both simulations give results almost similar to the simulation with the baseline model. These results indicate that the effect of the junction pressure drop and the vessels elasticity do not stack up when combined. Indeed, the elasticity decreases the resistance built up by the junction pressure drop relaxing the vessel walls across the network. In this comparison setup, both nonlinearities play an essential role in describing blood regulation in the organ.

3.2.3. Linear model

This model is the fully linear setup based on equations (2.1), (2.4), (2.10), (2.12) and (2.13). The total resistance in this model was lower compared to the above models, thus allowing a larger volumetric blood flow (table 2). The arterial structure provided 77.1% of the total resistance and venous structure 20.9%, the Darcy compartments contributing only 1.0% and 1.0% of the total value. This is a notable change in resistance distribution compared to the partial models and the baseline model. The total resistance was reduced by 6.3% with respect to the baseline model. This result is consistent with another independent study [19], in which it was found that the average resistance underestimation using a fully linearized one-dimensional blood flow model was in the range 4.6–6.4% for human cerebral networks modelling. These findings indicate that, by removing all nonlinearities, both the total resistance and the resistance distribution of the system are altered (table 3) .

3.3. Occlusion in root vessels

In this section, we demonstrate how our model framework can be applied to understand the blood flow regulation due to pathology or network alterations. A series of simulations were performed by occluding one root vessel at a time, in each network. The occlusions were in a range between 5% and 100% of the original vessel radius (figure 6). When the occlusion reaches 80% of the initial radius value, the resistance becomes almost constant, for both arteries and veins, and for both baseline and linear models. The

Table 3. Comparison of results of occlusion experiments in the literature. We cite excerpts from the original text.

object	method	artery occlusion	vein occlusion
One of the inlet or outlet vessels in a frog tongue (this work)	Simulation	The pressure above the occluded part of the structure was notably lower than the rest.	The existence of collateral circulation provided a new drain to maintain blood circulation after venous occlusions. The vascular structure played a vital role in the flow regulation.
One penetrating vessel in a human cortex model [2]	Simulation	'The central region of reduced blood pressure forms a conical shape, with the area of the region getting smaller with depth until the deep layers exhibit very little pressure drop'. 'The drop in flow affects a larger volume of tissue, spreading out further and deeper than the drop in blood pressure'. 'The micro-infarct volume dependence on vessel diameter is observed'.	'The results are similar to those for the arterioles, with conical pressure change regions, except that when occluding the venule there is a conical pressure increase as opposed to a decrease'. 'The drops in flow however are still diffuse across the voxel'.
A single vessel of penetrating arterioles or venules in a rat cortex [46]	Experiment	'An occlusion of either a penetrating arteriole or venule generated severely hypoxic conditions in the acute period of 6 h post-occlusion'. 'The occlusion of a single penetrating arteriole leads to a highly localized, nominally cylindrical region of tissue infarction over a course of 7 d'.	'The chronic result of occlusion to a penetrating venule is unreported and not readily predicted, as penetrating venules outnumber arterioles in rodent cortex and are highly collateralized on the pial surface'. 'Indeed, occlusion of a penetrating venule generated a microinfarction with notable similarity to that caused by occlusion of a penetrating arteriole'.
A single vessel of penetrating arterioles or venules in a mice cortex [47]	Experiment	'The experimental data for both penetrating arterioles and venules showed a complete or near complete cessation of flow close to the occlusion, whereas our calculated values were small, but non-zero (figure 7*d*,*f*). This discrepancy originates from the assumed linear relation of flux and pressure, which ignores the propensity of red blood cells to stall at low pressure differences.'	
A single vessel of penetrating arterioles in the rat cortex [48]	Experiment	'We found no evidence for active vasodilation in neighbouring arterioles in response to a penetrating arteriole occlusion'. 'We observed a slight, but not statistically significant, drop in both RBC speed and in RBC flow in neighbouring penetrating arterioles after the occlusion, indicating that blood flow to the area surrounding the occlusion was mildly decreased'. 'Uniformly over a 250 μm radius region around the occluded vessel, closely connected vessels dilated to a median diameter of 111% of baseline, whereas distantly connected vessels did not dilate'.	
A gerbil superior sagittal sinus (SSS) of the rat cortex (the observation of the venous network alteration) [49]	Experiment	'The angiography regularly revealed complex venous collateral pathways and venous flow reversal after SSS ligation, but demonstrated no significant differences in the diameter between that at pre-ligation and at 120 min post-SSS ligation'. 'The anatomical structure and an opening of the collateral pathways of the venous drainage system are closely related to microcirculatory alterations after venous occlusion'.	
An ascending venule and surface venule occlusion in the rat neocortex [50]	Experiment	'The median RBC speed in measured capillaries located within 100 μm of the occluded ascending venule decreased to approximately 26% of the baseline value, and returned to baseline with increasing distance from the occluded vessel'. 'We observed dramatic changes in the routing of blood flow through the capillary bed after AV occlusion'. 'We found that capillaries up to three branches upstream from the targeted venule dilated after the clot as compared with sham experiments, with an average diameter increase of approximately 25%'. 'Collateral surface venules, when present, helped maintain normal blood flow after surface venule occlusions'. 'Topological architecture had a large role in determining blood flow changes'.	

royalsocietypublishing.org/journal/rsos *R. Soc. Open Sci.* **8**: 201949

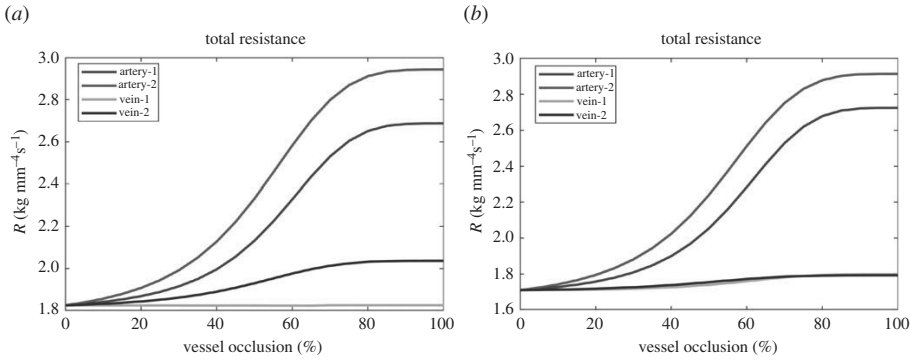

Figure 6. The vascular system resistance R as a function of the occlusion rate in vessels: (*a*) Resistance estimates for occlusions, *baseline model*. (*b*) Resistance estimates for occlusions, *linear model*. The occlusion rate (x-axis) in a vessel varies from 5% to 100% of the original radius for each simulation. Arteries 1 and 2 refer to a segment in the right and left big vessel of the arterial structure. Veins 1 and 2 refer to a segment in the right and left big vessel of the venous structure. The artery occlusions cause an increment of the macroscopic flow resistance in the whole system for both the baseline and linear models. For the vein 1 occlusion, the entire vascular resistance is almost constant ($\pm$3% of the original total resistance). By contrast, the increment of the total resistance in vein 2 occlusion shows that the vein 2 plays vital role in draining blood from the organ tissue. This effect is only observed in the nonlinear simulation, while the linear model failed to capture this anomaly.

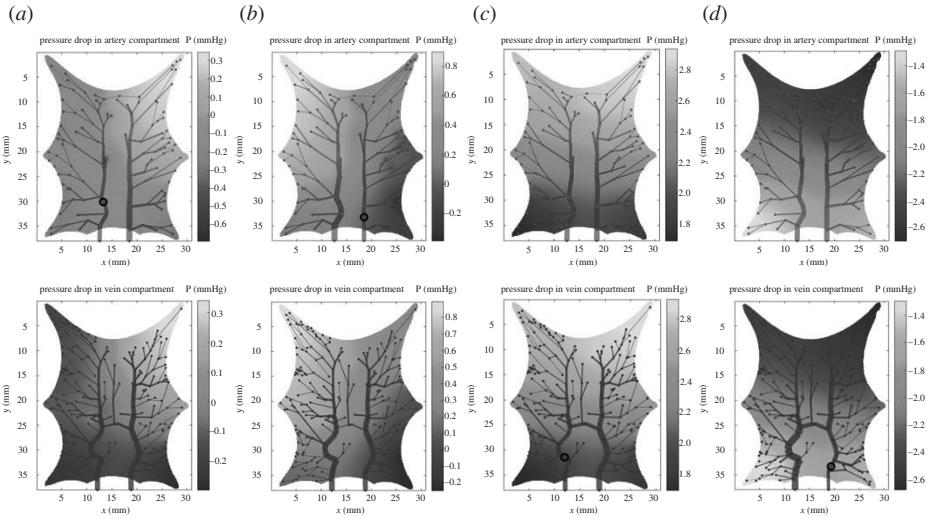

Figure 7. Pressure drop distribution in the capillary compartments with simulated occlusions (marked by black circle) computed with the baseline model. (*a*,*b*) Pressure drop distribution for artery occlusions are not mirroring each other due to the asymmetric structure of the arterial network with artery 1 occlusion generated bigger pressure drop. (*c*) Even with a negligible change in the macroscopic pressure drop (table 2), the pressure drop distribution in vein 1 experiment shows a notable pressure drop distribution for both compartments. (*d*) A higher pressure gradient between several terminal nodes in the bottom right corner enhances blood flow through the venous vessel rather than in the venous capillary. This microscopic alteration can occur with small change in the macroscopic flow.

occlusion experiments in the baseline model take considerably longer to run than the non-occluded experiments, due to the time required to achieve convergence in the nonlinear system (2.21). The occlusion location and the initial values determined using the linear model solution may be the cause of the large difference in convergence time (table 2).

3.3.1. Artery occlusion

Artery 1 and artery 2 occlusions generated expected results, increasing total resistances for both the occlusion on the baseline model and the linear model. The pressure above the occluded part of the

structure was notably lower than the rest. Furthermore, the artery 1 occlusion caused a steeper pressure gradient (left to right) compared to the artery 2 occlusion (figure 7*a*,*b*). This is due to the asymmetric structure of the left and right of the arterial network.

Table 2 reports a summary of the occlusion experiments with both baseline and linear models. Note that occlusions in the arterial roots increase resistance in the arterial structure and decrease total flow into the system. The driving pressure has to be raised around 20% compared to the non-occluded model to keep a similar volumetric blood flow. The artery 2 occlusion had a higher total resistance because the artery 2 vessel provides 16% more blood flow compared to the artery 1 vessel in the baseline model (figure 5). It shows that a prior higher blood flow in the occluded vessel will, in general, cause a more severe change to the system resistance. For artery occlusions, the linear model performs similarly to the baseline model, particularly for fully occluded vessels.

Figure 7 shows the pressure drop in the capillary compartments. Experimental studies of penetrating arteriole occlusion demonstrate similar effects. Table 3 summarizes the comparison between our findings and previous studies in the occlusion experiment. The observation in [46] reports a pressure drop in a region close to the occluded vessel and tissue hypoxia was detected in 6 h post-occlusion. The impact of vessel occlusion in penetrating arterioles in animal and human cortex has been studied both experimentally and numerically [2,46–48,51]. Although the two-dimensional frog tongue in this work differs extensively in terms of anatomical and functional properties to the cerebral cortex, the results show a good agreement for artery occlusion. In our simulation set-up, with only a pair of arteries and veins penetrating the capillary bed, the occlusion of one of the two main vessels had a more notable effect than for one vessel occlusion in the cerebral cortex, having instead several penetrating arterioles and venules [2,46].

3.3.2. Vein occlusion

The numerical results for the occluded venous networks show that the resistance changes for vein 1 and vein 2 occlusions had different character. While the vein 1 occlusion resulted in an almost constant total resistance, the vein 2 occlusion provided a resistance increase.

For the vein 1 occlusion, the total resistance only changed around $\pm 3\%$ of the baseline model, regardless of the occlusion percentage. This was due to vein 2 having 4.3 times more blood flow than vein 1, so that blood was drained from the vein compartment mainly through the vein 2 vessel. We also observed that the downstream vessels from the occlusion point were able to support blood influx from nearby terminals with an almost constant volumetric flow. In the converse situation, the vein 1 vessel could not support the blood flow when the vein 2 vessel was collapsed.

The vein 2 occlusion effects were consistent with venule occlusion in [2]. It generated a notable total resistance compared to the arteriole occlusion, except the capillary pressure increased instead of decreasing. In our simulation, the pressure drop in the vein 2 occlusion is less than for the artery occlusions (figure 7).

The simulated occlusions, both in arteries and veins, had a detectable impact to the blood circulation in general. These results are in good agreement with the experimental result on occlusions of one penetrating arterioles and venules in rats cortex (table 3) [46].

Without being necessarily physiologically consistent, the linear and baseline models occlusion results for vein 1 illustrate the models' capability to account for collateral circulation effects. A finer tuning of the modelling parameters may enable the system to maintain a close-to-constant net flow in varying anatomical setups. Yet, the present structure of the venous network has a good collateral circulation and maintains blood circulation in the whole system. This condition was mainly supported by the existence of anastomosis in the form of a big connected vessel in the venous network system, that allows flow across both sides of the vein network. These phenomena were consistent with the experimental result in [50], which showed that occlusion of one surface venule left the system's blood regulation almost unchanged when a collateral vessel provided a new drain.

Our vessel occlusion experiments do not take into account possible anatomical auto-regulating changes that can occur in the system over time. After a certain period, a real vascular system may change or heal to compensate for a blood circulation imbalance. This is a limitation of the model at present. An adaption of the model to allow for vessel tree growth would be highly interesting for instance in infarction modelling, but it is outside the main scope of this paper.

The resulting pressure distribution change in the venous compartment allows for blood going through the veins more than once and thereby also causes reduced blood flow in the capillary bed. Figure 7*d* shows an example of blood flow in the reverse direction due to a high-pressure difference

in the venous Darcy compartment. Higher pressure gradients between several terminal nodes in the bottom left corner make blood flow through venous vessels rather than in the capillary bed. In the vein 2 occlusion, around 5% of blood flow direction in the venous vessels was reversed, 28% of venous vessels had an average 23% blood flow increase, while the remaining vessels had a decrease of 16%. This result was also shown in the experimental result in the venule occlusion [50]: cortical ascending venules occlusions caused blood flow decrease and reversed flow direction (table 3). They also observed a radius dilation up to 25%, while the radii dilation in our simulation was less than 5%. The simulation design and parameters are crucial in determining vessel change, which may allow for greater radius dilation similar to experimental values.

4. Conclusion

We have introduced a nonlinear multi-scale modelling framework incorporating important features of blood flow in a full organ vasculature. The model is demonstrated using a two-dimensional geometry domain and vasculature from a frog tongue [23]. Our numerical experiments indicate that the modelling complexity is sufficient to account for important physiological and structural features. The combination of the explicit vessel representation and a generic Darcy model representation yields realistic full-organ simulations, without having a detailed knowledge of the local microvasculature. The framework is also highly flexible allowing for inclusion of other local nonlinear processes.

In the numerical experiments, the baseline simulations are in good agreement with empirical data from a male frog *Rana pipiens* mesentery [24]. Further, we conduct simulations with a pressure drop distribution in the whole vasculature consistent with the average distribution in other animals as well as humans [25,43,44]. The linearized simulations indicate the nonlinearities have an impact on the system. The simulations with partial models suggest that the nonlinear effects of vessel elasticity and pressure drop at vessel junctions do not stack up when combined, indicating that the two compensate for each other.

We illustrate the modelling potential by applying the method to vascular occlusions. Vessel networks alteration simulations confirm that both local and global blood circulations in the vascular system depend on the vascular structure. In our simulations, the existence of an anastomosis in form of a big connected vessel in the venous network system has an important role in maintaining blood circulation when a main root is occluded. We illustrate how an occlusion in the venous structure alters the microscopic flow resistance, while at the same time has negligible effects on the macroscopic flow.

Our simulations indicate that it is important to simulate the complete vascular system including the venous system, and not just the arterial system. In line with [50], our results of the venous occlusion experiments emphasize the importance of introducing elasticity and nonlinearities to provide a more accurate simulation of the blood flow.

Data accessibility. Data available on https://doi.org/10.5061/dryad.pg4f4qrn2.

Authors' contributions. All authors participated in the study design. U.Q. drafted the early version of the manuscript, and A.Z.M.K., J.M.N. and E.A.H. assessed and discussed the mathematical formulation and analysis of the methods. U.Q. drafted the figures. All authors edited the manuscript and approved the final version.

Competing interests. We declare we have no competing interests.

Funding. This work was supported by the Research Council of Norway under Frinatek 'Flow-based interpretation of dynamic contrast-enhanced MRI' project (NFR no. 262203).

References

1. Black S, Ritos K, Maclean C, Brodie R, Kazakidi A. 2020 P14 blood flow analysis of the aortic arch using computational fluid dynamics in a coupled 3D-0D framework. *Heart* **106**, A10–A11. (doi:10.1136/heartjnl-2019-314898)
2. El-Bouri WK, Payne SJ. 2018 Investigating the effects of a penetrating vessel occlusion with a multi-scale microvasculature model of the human cerebral cortex. *NeuroImage* **172**, 94–106. (doi:10.1016/j.neuroimage.2018.01.049)
3. Hodneland E *et al.* 2019 A new framework for assessing subject-specific whole brain circulation and perfusion using MRI-based measurements and a multi-scale continuous flow model. *PLoS Comput. Biol.* **15**, 1–31. (doi:10.1371/journal.pcbi.1007073)
4. Olufsen MS, Nadim A, Lipsitz LA. 2002 Dynamics of cerebral blood flow regulation explained using a lumped parameter model. *Am. J. Physiol.-Regul. Integr. Comp. Physiol.* **282**, R611–R622. (doi:10.1152/ajpregu.00285.2001)
5. Passerini T, Luca Md, Formaggia L, Quarteroni A, Veneziani A. 2009 A 3D/1D geometrical multiscale model of cerebral vasculature. *J. Eng. Math.* **64**, 319. (doi:10.1007/s10665-009-9281-3)
6. Perdikaris P, Grinberg L, Karniadakis GE. 2016 Multiscale modeling and simulation of brain blood flow. *Phys. Fluids* **28**, 021304. (doi:10.1063/1.4941315)
7. Peyrounette M, Davit Y, Quintard M, Lorthois S. 2018 Multiscale modelling of blood flow in cerebral microcirculation: details at capillary scale control accuracy at the level of the cortex. *PLoS ONE* **13**, 1–35. (doi:10.1371/journal.pone.0189474)
8. Quarteroni A, Veneziani A, Vergara C. 2016 Geometric multiscale modeling of the cardiovascular system, between theory and

practice. *Comput. Methods Appl. Mech. Eng.* **302**, 193–252. (doi:10.1016/j.cma.2016.01.007)

9. Qureshi MU, Vaughan GDA, Sainsbury C, Johnson M, Peskin CS, Olufsen MS, Hill NA. 2014 Numerical simulation of blood flow and pressure drop in the pulmonary arterial and venous circulation. *Biomech. Model. Mechanobiol.* **13**, 1137–1154. (doi:10.1007/s10237-014-0563-y)
10. Reichold J, Stampanoni M, Keller AL, Buck A, Jenny P, Weber B. 2009 Vascular graph model to simulate the cerebral blood flow in realistic vascular networks. *J. Cereb. Blood Flow Metab.* **29**, 1429–1443. (doi:10.1038/jcbfm.2009.58)
11. Blanco P, Pivello M, Urquiza S, Feijóo R. 2009 On the potentialities of 3D-1D coupled models in hemodynamics simulations. *J. Biomech.* **42**, 919–930. (doi:10.1016/j.jbiomech.2009.01.034)
12. Rohan E, Lukeš V, Jonášová A. 2018 Modeling of the contrast-enhanced perfusion test in liver based on the multi-compartment flow in porous media. *J. Math. Biol.* **77**, 421–454. (doi:10.1007/s00285-018-1209-y)
13. Cookson A, Lee J, Michler C, Chabiniok R, Hyde E, Nordsletten D, Sinclair M, Siebes M, Smith N. 2012 A novel porous mechanical framework for modelling the interaction between coronary perfusion and myocardial mechanics. *J. Biomech.* **45**, 850–855. (doi:10.1016/j.jbiomech.2011.11.026)
14. Lee J, Nordsletten D, Cookson A, Rivolo S, Smith N. 2016 In silico coronary wave intensity analysis: application of an integrated one-dimensional and poromechanical model of cardiac perfusion. *Biomech. Model. Mechanobiol.* **15**, 1535–1555. (doi:10.1007/s10237-016-0782-5)
15. Blanco P, Feijóo R, Urquiza S. 2007 A unified variational approach for coupling 3D-1D models and its blood flow applications. *Comput. Methods Appl. Mech. Eng.* **196**, 4391–4410. (doi:10.1016/j.cma.2007.05.008)
16. Moghadam ME, Vignon-Clementel IE, Figliola R, Marsden AL. 2013 A modular numerical method for implicit 0D/3D coupling in cardiovascular finite element simulations. *J. Comput. Phys.* **244**, 63–79. Multi-scale Modeling and Simulation of Biological Systems. (doi:10.1016/j.jcp.2012.07.035)
17. El-Bouri WK, Payne SJ. 2015 Multi-scale homogenization of blood flow in 3-dimensional human cerebral microvascular networks. *J. Theor. Biol.* **380**, 40–47. (doi:10.1016/j.jtbi.2015.05.011)
18. Shipley RJ, Smith AF, Sweeney PW, Pries AR, Secomb TW. 2019 A hybrid discrete-continuum approach for modelling microcirculatory blood flow. *Math. Med. Biol.: J. IMA* **37**, 40–57.
19. Chnafa C, Valen-Sendstad K, Brina O, Pereira V, Steinman D. 2017 Improved reduced-order modelling of cerebrovascular flow distribution by accounting for arterial bifurcation pressure drops. *J. Biomech.* **51**, 83–88. (doi:10.1016/j.jbiomech.2016.12.004)
20. Mynard JP, Valen-Sendstad K. 2015 A unified method for estimating pressure losses at vascular junctions. *Int. J. Numer. Methods Biomed. Eng.* **31**. (doi:10.1002/cnm.v31.7)
21. van de Vosse FN, Stergiopulos N. 2011 Pulse wave propagation in the arterial tree. *Annu. Rev. Fluid Mech.* **43**, 467–499. (doi:10.1146/fluid.2011.43.issue-1)
22. Burggren WW, Bicudo JE, Glass ML, Abe AS. 1992 Development of blood pressure and cardiac reflexes in the frog *Pseudis paradoxsus*. *Am. J. Physiol.-Regul. Integr. Comp. Physiol.* **263**, R602–R608. (doi:10.1152/ajpregu.1992.263.3.R602)
23. Cohnheim JF. 1872 *Untersuchungen über die embolischen prozesse*. Berlin, Germany: Hirschwald.
24. Gore RW. 1972 Wall stress: a determinant of regional differences in response of frog microvessels to norepinephrine. *Am. J. Physiol. Legacy Content* **222**, 82–91. (doi:10.1152/ajplegacy.1972.222.1.82)
25. Landis EM. 1931 Capillary pressure and hyperemia in muscle and skin of the frog. *Am. J. Physiol.-Legacy Content* **98**, 704–716. (doi:10.1152/ajplegacy.1931.98.4.704)
26. Doyen PM. 1988 Permeability, conductivity, and pore geometry of sandstone. *J. Geophys. Res.: Solid Earth* **93**, 7729–7740. (doi:10.1029/JB093iB07p07729)
27. Peterson LH, Jensen RE, Parnell J. 1960 Mechanical properties of arteries *in vivo*. *Circ. Res.* **8**, 622–639. (doi:10.1161/01.RES.8.3.622)
28. Caro CG, Pedley T, Schroter R, Seed W. 2012 *The mechanics of the circulation*. Cambridge, UK: Cambridge University Press.
29. Pries A, Secomb TW, Gaehtgens P. 1996 Biophysical aspects of blood flow in the microvasculature. *Cardiovasc. Res.* **32**, 654–667. (doi:10.1016/S0008-6363(96)00065-X)
30. Morales HG, Larrabide I, Geers AJ, Aguilar ML, Frangi AF. 2013 Newtonian and non-Newtonian blood flow in coiled cerebral aneurysms. *J. Biomech.* **46**, 2158–2164. (doi:10.1016/j.jbiomech.2013.06.034)
31. Pries AR, Secomb TW, Gaehtgens P, Gross J. 1990 Blood flow in microvascular networks: experiments and simulation. *Circ. Res.* **67**, 826–834. (doi:10.1161/01.RES.67.4.826)
32. Perkkiö J, Keskinen R. 1983 Hematocrit reduction in bifurcations due to plasma skimming. *Bull. Math. Biol.* **45**, 41–50. (doi:10.1016/S0092-8240(83)80040-8)
33. Possenti L, di Gregorio S, Gerosa FM, Raimondi G, Casagrande G, Costantino ML, Zunino P. 2019 A computational model for microcirculation including Fahraeus-Lindqvist effect, plasma skimming and fluid exchange with the tissue interstitium. *Int. J. Numer. Methods Biomed. Eng.* **35**, e3165. (doi:10.1002/cnm.v35.3)
34. Payne SJ. 2017 *Cerebral blood flow and metabolism: a quantitative approach*. Singapore: World Scientific.
35. Darcy H. 1856 Les fontaines publiques de la ville de Dijon: exposition et application.... Paris, France: Victor Dalmont.
36. Hodneland E, Hu X, Nordbotten JM. 2020 Modeling, well-posedness and discretization for a class of models for mixed-dimensional problems with high dimensional gap.
37. Aavatsmark I. 2007 Interpretation of a two-point flux stencil for skew parallelogram grids. *Comput. Geosci.* **11**, 199–206. (doi:10.1007/s10596-007-9042-1)
38. Powell MJ. 1968 A Fortran subroutine for solving systems of nonlinear algebraic equations. Technical report Atomic Energy Research Establishment, Harwell, England, UK.
39. Qohar UNA, Hanson EA, Munthe-Kaas AZ, Nordbotten JM. 2021 Frog tongue segmentation data for a realistic vascular structure in modelling. (doi:10.5061/dryad.pg4f4qrn2).
40. Hanson EA, Lundervold A. 2013 Local/non-local regularized image segmentation using graph-cuts. *Int. J. Comput. Assist. Radiol. Surg.* **8**, 1073–1084. (doi:10.1007/s11548-013-0903-x)
41. Moalli R, Meyers RS, Jackson DC, Millard RW. 1980 Skin circulation of the frog, *Rana catesbeiana*: distribution and dynamics. *Respir. Physiol.* **40**, 137–148. (doi:10.1016/0034-5687(80)90088-2)
42. Söderström-Lauritzsen V, Nilsson GE, Lutz PL. 2001 Effect of anoxia and adenosine on cerebral blood flow in the leopard frog (*Rana pipiens*). *Neurosci. Lett.* **311**, 85–88. (doi:10.1016/S0304-3940(01)02136-X)
43. Golub A, Ivanova S, Shoshenko K. 1978 Blood supply in the arterial and venous bed of submaxillary muscle of frogs. *Fiziol. Zh. Im. I M Sechenova* **64**, 508–509.
44. Landis EM. 1930 The capillary blood pressure in mammalian mesentery as determined by the micro-injection method. *Am. J. Physiol.-Legacy Content* **93**, 353–362. (doi:10.1152/ajplegacy.1930.93.1.353)
45. Gould IG, Tsai P, Kleinfeld D, Linninger A. 2017 The capillary bed offers the largest hemodynamic resistance to the cortical blood supply. *J. Cereb. Blood Flow Metab.* **37**, 52–68. (doi:10.1177/0271678X16671146)
46. Shih AY, Blinder P, Tsai PS, Friedman B, Stanley G, Lyden PD, Kleinfeld D. 2013 The smallest stroke: occlusion of one penetrating vessel leads to infarction and a cognitive deficit. *Nat. Neurosci.* **16**, 55–63. (doi:10.1038/nn.3278)
47. Blinder P, Tsai PS, Kaufhold JP, Knutsen PM, Suhl H, Kleinfeld D. 2013 The cortical angiome: an interconnected vascular network with noncolumnar patterns of blood flow. *Nat. Neurosci.* **16**, 889–897. (doi:10.1038/nn.3426)
48. Nishimura N, Rosidi NL, Iadecola C, Schaffer CB. 2010 Limitations of collateral flow after occlusion of a single cortical penetrating arteriole. *J. Cereb. Blood Flow Metab.* **30**, 1914–1927. (doi:10.1038/jcbfm.2010.157)
49. Ueda K, Nakase H, Miyamoto K, Otsuka H, Sakaki T. 2000 Impact of anatomical difference of the cerebral venous system on microcirculation in a gerbil superior sagittal sinus occlusion model. *Acta Neurochir. (Wien)* **142**, 75–82. (doi:10.1007/s007010050010)
50. Nguyen J, Nishimura N, Fetcho RN, Iadecola C, Schaffer CB. 2011 Occlusion of cortical ascending venules causes blood flow decreases, reversals in flow direction, and vessel dilation in upstream capillaries. *J. Cereb. Blood Flow Metab.* **31**, 2243–2254. (doi:10.1038/jcbfm.2011.95)
51. Nishimura N, Schaffer CB, Friedman B, Lyden PD, Kleinfeld D. 2007 Penetrating arterioles are a bottleneck in the perfusion of neocortex. *Proc. Natl Acad. Sci. USA* **104**, 365–370. (doi:10.1073/pnas.0609551104)

Graphic design: Communication Division, UiB / Print: Skipnes Kommunikasjon AS

uib.no

ISBN: 9788230866382 (print)
9788230846117 (PDF)